frontiers in Earth Science

ORIGINAL RESEARCH
published: 15 June 2021
doi: 10.3389/feart.2021.682720

Zircon Genesis and Geochronology for the Zhangbaoshan Super-Large Rubidium Deposit in the Eastern Tianshan, NW China: Implication to Magmatic-Hydrothermal Evolution and Mineralization Processes

Jun Zhi[1], Ruxiong Lei[2], Boyang Chen[1], M. N. Muhtar[1], Zhijie Feng[1], Kai Zhang[2], Yuanfeng Cai[1] and Changzhi Wu[2,3]*

[1]State Key Laboratory for Mineral Deposits Research, School of Earth Sciences and Engineering, Nanjing University, Nanjing, China, [2]School of Earth Science and Resources, Chang'an University, Xi'an, China, [3]Xinjiang Research Centre for Mineral Resources, Chinese Academy of Sciences, Urumqi, China

OPEN ACCESS

Edited by:
Massimo Chiaradia, Université de Genève, Switzerland

Reviewed by:
Nuo Li, Leibniz Universität Hannover, Germany
Mohsen Rezaei, Shahid Chamran University of Ahvaz, Iran

***Correspondence:**
Ruxiong Lei
ruxionglei@chd.edu.cn

Specialty section:
This article was submitted to Economic Geology, a section of the journal Frontiers in Earth Science

Received: 19 March 2021
Accepted: 31 May 2021
Published: 15 June 2021

Citation:
Zhi J, Lei R, Chen B, Muhtar MN, Feng Z, Zhang K, Cai Y and Wu C (2021) Zircon Genesis and Geochronology for the Zhangbaoshan Super-Large Rubidium Deposit in the Eastern Tianshan, NW China: Implication to Magmatic-Hydrothermal Evolution and Mineralization Processes. Front. Earth Sci. 9:682720. doi: 10.3389/feart.2021.682720

The Zhangbaoshan (ZBS) super-large Rubidium deposit, located in the Eastern Tianshan, is a typical granite-type Rb deposit. The ZBS deposit is mainly hosted in the highly evolved Baishitouquan (BST) pluton enriched in F and Rb, which exhibits five lithological zones from the bottom to the top: leucogranite (zone-a), amazonite-bearing granite (zone-b), amazonite granite (zone-c), topaz-bearing amazonite granite (zone-d) and topaz albite granite (zone-e), as well as minor small lodes of amazonite pegmatite. Two types of zircon were identified from the BST pluton. Type-I zircons mainly occur in the zone–a, are characterized by obvious oscillatory zoning, high Zr contents (47.4–67.3 wt% ZrO_2) and Zr/Hf ratios (21.72–58.23), low trace element concentrations, and heavy rare earth elements (HREE)–enriched patterns with prominent positive Ce anomalies (Ce/Ce* = 1.21–385) and strong negative Eu anomalies (Eu/Eu* = 0.008–0.551), indicative of early magmatic zircon. Type–II zircons mainly occur in the upper zones (zone-c to zone-e), exhibit porous and dark Cathodoluminescence images, inhomogeneous internal structure, plenty of mineral inclusions, low Zr (38.7–51.0 wt% ZrO_2) and Zr/Hf ratios (3.35–11.00), high Hf (34,094–85,754 ppm), Th (718–4,980 ppm), U (3,540–32,901 ppm), Ta (86.7–398 ppm), Y (1,630–28,890 ppm) and rare earth elements (REEs) (3,910–30,165 ppm), as well as slightly HREE–enriched patterns and significant M–type tetrad patterns with t_3 values (quantification factor of tetrad effect) of 1.51–1.69. It is suggested that the type–II zircons are crystallized from a deuteric F–rich fluid coexisted with the highly evolved residual magma during the transition from the magmatic to the F–rich hydrothermal stage of the BST pluton. The F–rich fluid exsolution during the magmatic–hydrothermal transition is one of the most important factors controlling the modification of highly evolved granite and related Rb enrichment and mineralization. The type–I zircon samples from zone–a yield concordant ages of 250 ± 2.5 Ma and 250.5 ± 1.7 Ma, respectively, indicating that the BST pluton was emplaced

in the Early Triassic. The type–II zircons from zone–c to zone–e yield lower intercept U–Pb ages between 238 and 257 Ma, which may represent the age of F–rich fluid–melt interaction during the transition from the magmatic to the hydrothermal stage. The mineralization of the ZBS super–large Rb deposit should have occurred shortly after emplacement of the BST pluton in the Early Triassic. Combined with available data, it is suggested that the Triassic is an important period for granitic magmatism and rare metal metallogeny in the Eastern Tianshan.

Keywords: rubidium deposit, f-rich highly evolved granite, hydrothermal zircon, zircon alteration, Eastern tianshan

INTRODUCTION

As a common accessory mineral in a variety of rocks, zircon has long been recognized as an excellent geochronometer due to its high U, Th and low common Pb contents, and high closure temperature for the U–Th–Pb system (Geisler et al., 2007; Harley et al., 2007). Zircon can also incorporate considerable amounts of temperature–or process–sensitive trace elements, including Hf, Y, Ti and REEs during crystallization, which make it a useful tool to fingerprint the mineral–melt–fluid processes during crust formation and evolution, hydrothermal alteration and mineralization (Belousova et al., 2006; Geisler et al., 2007; Hanchar and Van Westrenen, 2007; Harley et al., 2007).

Zircon is ubiquitous in granitoids and has generally been considered as magmatic in origin (e.g., Hoskin, 2005; Jiang et al., 2020). However, zircons of both magmatic and hydrothermal origin commonly occur in highly evolved granite and pegmatite (e.g., Yang et al., 2014; Li H. et al., 2018; Li X.-C. et al., 2018; Huang et al., 2020). In addition, recent studies have suggested that zircons are susceptible to hydrothermal alterations (Erdmann et al. 2013; Yang et al., 2014; Li and Zhou, 2015; Takehara et al., 2018; Liu et al., 2019), and the crystal structure, chemical composition and isotopic system of zircons could be disturbed during hydrothermal alteration processes, including recrystallization, dissolution–reprecipitation and metamictization (Geisler et al., 2007; Kusiak et al., 2009). Zircon has been proved to be modified by F–rich fluids (Veksler et al., 2005; Han et al., 2019), and Zr and trace elements (e.g., REEs, Ta, Ti, Hf, Th, and U) within zircon have been suggested to be mobile in alkali–and F–rich highly evolved magmatic systems (Veksler et al., 2005; Ayers et al., 2012). Therefore, zircons in F–rich highly evolved magmatic systems are generally complex, and caution should be taken to interpret their elemental and isotopic data.

The Zhangbaoshan (ZBS) super–large rubidium deposit is a typical granite–type Rb deposit, which is mainly hosted in the highly evolved Baishitouquan (BST) pluton and partly in the other pluton around the BST in the Eastern Tianshan, Northwest China (GPGSI, 2015). The BST pluton is characterized by high SiO_2, Na_2O, K_2O, Li, Rb, Cs and F, low Ti, Fe, Ca, and Mg contents, is weakly peraluminous (A/NKC = 1.00–1.11), and has low K/Rb, Al/Ga, Y/Ho, Zr/Hf and Nb/Ta ratios (Gu et al., 2003). It can be divided into five lithological zones based on the mineral compositions, which are considered to be formed by successive fractionation crystallization and F–rich fluid–melt interaction (Gu et al., 2011). Previous studies have mainly focused on the petrology and geochemical feature of the BST pluton (Gu et al., 2003; Gu et al., 2011; Wu et al., 2011), however, little attention has been paid to the associated Rb enrichment and mineralization mechanism. Although it is generally suggested that Rb mineralization is related to highly evolved granitic systems, our current understanding of the geological processes governing Rb mineralization is still limited and controversial (Han et al., 2021). Furthermore, the emplacement age of the BST pluton and the timing of the Rb mineralization are still unclear (Gu et al., 1994; Liu et al., 2008), which has hindered a better understanding of the formation of the granite and the Rb mineralization mechanism.

In this paper, we present new results of detailed petrographic characteristics, chemical composition and LA–ICP–MS U–Pb ages of zircons from each lithological zone of the BST pluton. Using these data, we identify two types of zircons and constrain their origin, which is crucial for correctly determine the age of granite emplacement and Rb mineralization. We also discuss the implications of our results for illustrating the magmatic and hydrothermal evolution process of the BST pluton and Rb deposit, which may provide new insights for the formation of Rb and F–rich highly evolved granites.

GEOLOGICAL BACKGROUND

The Central Asian Orogenic Belt (CAOB) is the world's largest Phanerozoic accretive orogenic belt, surrounded by the Siberian, European, Tarim and North China cratons (**Figure 1A**; Xiao et al., 2004; Jahn, 2004; Windley et al., 2007; Wang et al., 2014; Xiao et al., 2015; Li et al., 2017; Deng et al., 2017). The Eastern Tianshan is considered as the southernmost segment of the CAOB, located at the junction of the Junggar Block and Turfan–Hami Block (**Figure 1B**). From north to south, the Eastern Tianshan is composed of the Bogda–Harlik Arc, the Jueluotag Arc belt, and the Central Tianshan Block, respectively (**Figure 1C**; Coleman, 1989; Sengor et al., 1993; Xiao et al., 2004; Shu et al., 2011; Zhang et al., 2016).

The Bogeda–Harlik Arc is mainly composed of Ordovician–Carboniferous volcanic rocks, granites and mafic–ultramafic complexes (Gu et al., 2001). The Jueluotag Arc belt can be subdivided into three subunits from north to south, which are the Dananhu–Tousuquan Arc, the Kanggur Basin, and the Aqishan–Yamansu Arc, respectively (**Figure 1C**).

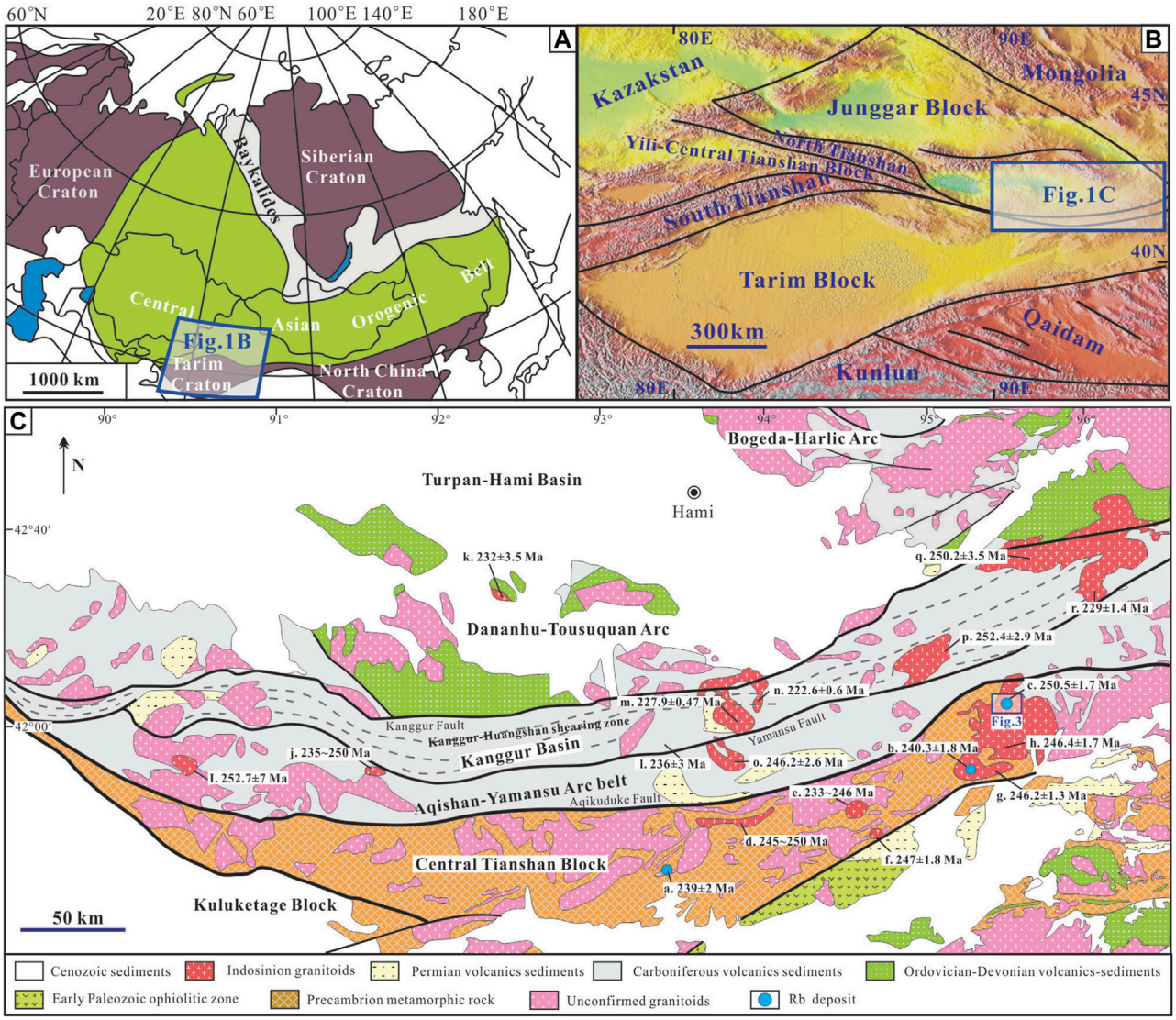

FIGURE 1 | (A) Tectonic sketch map of the Central Asian Orogenic Belt (modified from Sengor et al., 1993). **(B)** Topographic and tectonic sketch map of Xinjiang, Northwest China, and adjacent areas (modified from Muhtar et al., 2020a). **(C)** Geological map of the Eastern Tianshan (modified from Wang et al. (2006) and Deng et al. (2017)). (a–r represents dated Triassic granitoids and related metal deposits, please see name and reference information in **Supplementary Appendix Table 1**).

The Dananhu–Tousuquan Arc, north of the Kanggur Fault, mainly consists of Ordovician–Carboniferous volcanic and pyroclastic rocks and accretionary complexes (Xiao et al., 2004; Wang Y. et al., 2018; Muhtar et al., 2020b). The Kanggur Basin, located between the Kanggur Fault and Yamansu Fault, is mainly composed of Carboniferous volcanic–sedimentary rocks, with intense ductile shearing and a large right–lateral slip throughout the basin (Xu et al., 2003; Wu et al., 2018). The Aqishan–Yamansu Arc, south of the Yamansu Fault, mainly consists of Carboniferous volcanic, volcani-clastic, terrigenous clastic sedimentary rocks and limestones (Hou et al., 2014; Wang Y. et al., 2018). The Central Tianshan Block is mainly composed of Precambrion volcano–sedimentary rocks (Chen, 1999; Shu et al., 2004; Xiao et al., 2004; Lei et al., 2011). Most of these rocks have been metamorphosed to migmatized schists, gneisses, marbles and amphibolites (Hu et al., 1997).

The Eastern Tianshan has a wide distribution of magmatic rocks, which are mainly emplaced during the Paleozoic (e.g., Gu et al., 2006; Zhou et al., 2010; Chen et al., 2011; Zhang et al., 2014; Chen et al., 2019). Triassic granitoids have been identified in the Eastern Tianshan during the past decade and various Triassic granite–related W, Mo and Rb deposits have also been discovered in the Eastern Tianshan (shown in **Supplementary Appendix Table 1**). The mineralizing characteristics and zircon U-Pb ages of Rb-bearing granites in the Eastern Tianshan are listed in **Supplementary Appendix Table 2**. This suggests that the Triassic was an important magmatic and metallogenic period

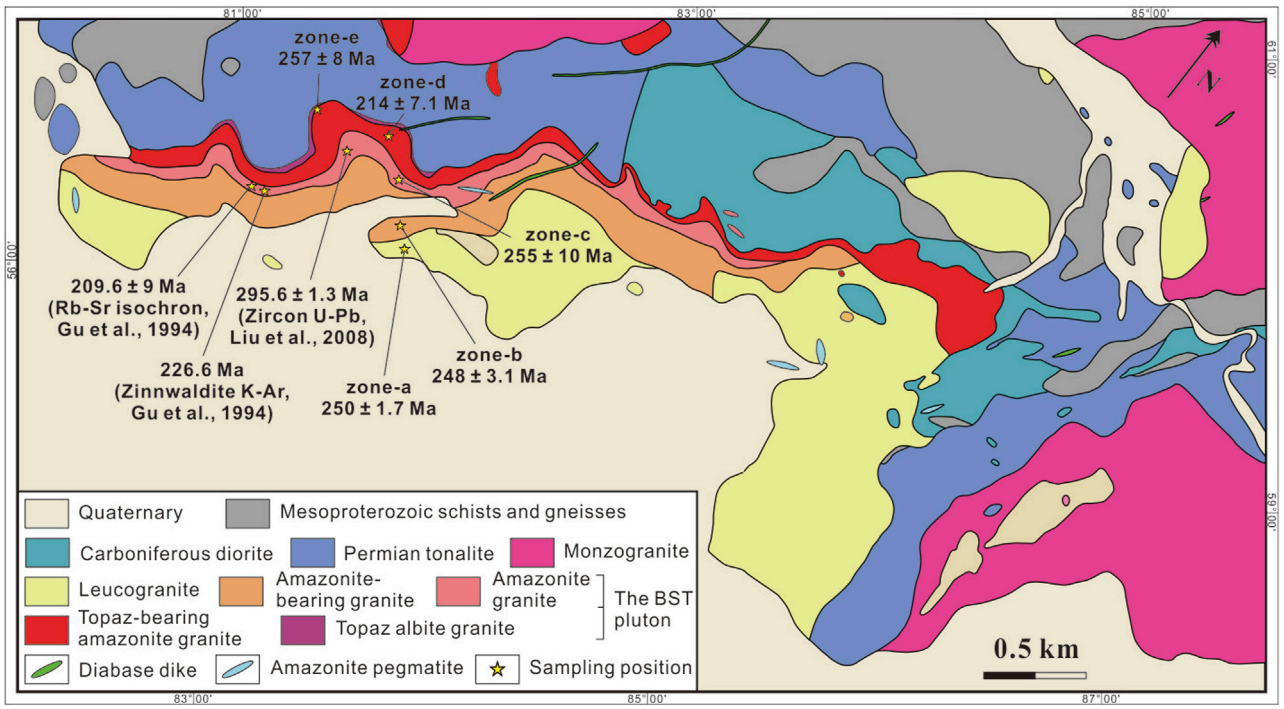

FIGURE 2 | Simplified geological map of the Baishitouquan (BST) in the Central Tianshan Block.

in the Eastern Tianshan (Wu et al., 2010; Deng et al., 2017; Zhang et al., 2017; Lei et al., 2020).

GEOLOGY OF THE ZHANGBAOSHAN RB DEPOSIT

The ZBS Rb deposit, located in the eastern section of the Central Tianshan Block, Eastern Tianshan, (**Figure 1C**), is a typical granite–type Rb deposit (GPGSI, 2015). Recent exploration identified that it is a super large Rb deposit, with ore reserves (Rb_2O) of about 67,080 tons (GPGSI, 2015). The main Rb–bearing minerals in the deposit are microcline (0.36–0.41 wt% Rb_2O) and zinnwaldite (0.35–0.67 wt% Rb_2O). The Rb deposit is mainly hosted by the BST pluton, which intruded into the Mesoproterozoic schists and gneisses and the Carboniferous diorite. The BST pluton exhibits intrusive contacts with the overlying Permian tonalite and monzogranite (**Figure 2**). Based on detailed petrological and mineralogical studies, the BST pluton can be divided into five progressive lithological zones from the bottom to the top, namely leucogranite (zone–a), amazonite–bearing granite (zone–b), amazonite granite (zone–c), topaz–bearing amazonite granite (zone–d) and topaz albite granite (zone–e) (Gu et al., 2003; Gu et al., 2011).

Leucogranite (zone–a) is weakly altered and ash gray in color, which is the main part of this pluton. This zone is mainly composed of plagioclase (22–36%), K–feldspar (25–35%), quartz (28–35%) and zinnwaldite (3–5%), exhibiting medium–to fine–grained texture and massive structure. The main difference between zone–b and zone–a is the occurrence of amazonite (2–5%), as well as microcline (2–5%). As the content of amazonite generally increases upwards from the zone–b to zone–c (mainly 5–15%, and up to 20%), the lithology gradually evolved from amazonite–bearing granite to amazonite granite (**Figure 3A**). Correspondingly, the content of microcline increases to 5–15% in zone–c, which is generally characterized by cross–hatched twinning (**Figure 3B**). The zone–d is characterized by the appearance of topaz (1–5%) in the form of phenocrysts, and the main composition of this zone is essentially similar to the amazonite granite (**Figure 3C**). The zone–e exhibits an abrupt transition with zone–d below: this zone mainly contains phenocrysts of topaz (10–20%) and quartz (15–30%), and matrix of albite (45–60%), K-feldspar (10–15%) and zinnwaldite (5–10%). Accessory minerals of the BST pluton mainly consists of zircon, fluorite, garnet, cassiterite, magnatite, apatite, monazite and columbite–group minerals.

Veins of the topaz albite granite (zone–e) cut and replace the overlying tonalite locally (**Figure 3D**). There are several amazonite pegmatite veins cutting through both the pluton and overlying tonalite (**Figure 3E**). These amazonite pegmatite veins show compositional zoning from a marginal fine–grained muscovite–feldspar zone to a central pegmatitic muscovite–quartz–microcline zone, with a thickness of 0.3–1 m and length of 2–10 m. The high concentration of volatiles (F and H_2O) in zone–e and the appearance of amazonite pegmatite veins indicate that the magmatic–hydrothermal transition stage has played an important role in the formation of the pluton (Gu et al., 2011).

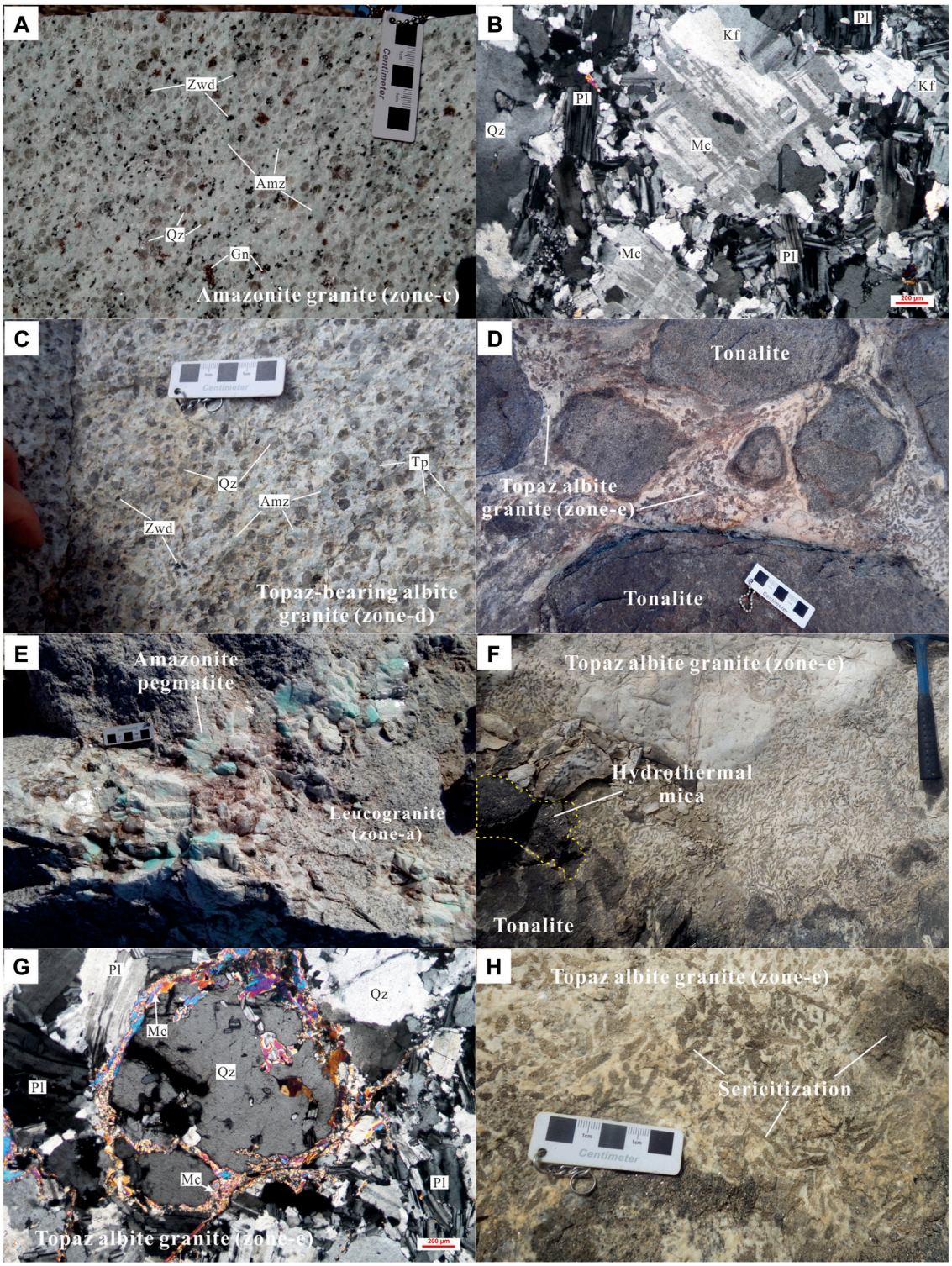

FIGURE 3 | Field photographs and microphotographs showing lithological characteristics of the BST pluton. Mineral symbols: Qz–quartz, Pl–albite, Kf–K-feldspar, Amz–amazonite, Zwd–zinnwaldite, Mc–microcline, Tp–topaz, Gn–garnets. **(A)** Porphyritic texture of amazonite granite from zone–c. Hand specimen. **(B)** Microphotograph showing the texture of amazonite granite. Microcline with cross–hatched twins has corroded K-feldspar and albite grains into optically continuous relict. Crossed polarizers. **(C)** Prismatic topaz crystals occur as a phenocrysts in zone–d. Hand specimen. **(D)** The zone–e has penetrated and replaced the overlying tonalite (country rock). **(E)** Amazonite pegmatite vein in zone–a. **(F)** Clustered crystals of hydrothermal mica occuring in the contact between the zone–e and tonalite. **(G)** White mica and twin-free albite occurring as vein along mineral grains and fractures in zone-e. **(H)** Prismatic topaz crystals were replaced by hydrothermal mica.

Hydrothermal alteration in the ZBS Rb deposit occurs mainly in zone-e, including muscovitization, sericitization, albitization, and fluoritization, which is principally represented by secondary fluorite, white mica and albite. White mica and twin-free albite replacing topaz and K-feldspar (**Figure 3F**) or occurring as veins along mineral grain and fractures in zone-e (**Figure 3G**) can be observed, indicating that they are produced by subsolidus metasomatism. Moreover, clustered crystals of hydrothermal mica with low Rb, Cs, Fe, Mn, Al and high Si, Ti, Mg contents (unpublished data) can be observed at the contact of zone–e and tonalite (**Figure 3H**), indicative of a hydrothermal origin.

SAMPLING AND ANALYTICAL METHODS

Zircons from seven samples from zone–a (BST–27, 19KH–231), zone–b (19KH–235), zone–c (19KH–238), zone–d (19KH–253), and zone–e (19KH–250, xxx–22), with sampling depth of 1,490 m, 1,498 m, 1,509 m, 1,540 m, 1,558 m, 1,521 m, 1,573 m, respectively, were extracted for zircon petrography observation, U–Pb dating, and trace element analyses.

The distribution and paragenesis of the zircons in the granite were examined in transmitted light using an optical microscope. Zircon grains from each sample were separated by gravity and magnetic methods, and mounted in one–inch epoxy resin disk. The internal structure of single zircon crystals was studied by Cathodoluminescence (CL) and Backscattered electron (BSE) imaging. The CL and BSE images were collected by using a JEOL JXA–8100 electron microprobe at the State Key Laboratory for Mineral Deposits Research (SKLMDR), Nanjing University (China), with operating conditions of 15 kV accelerating voltage and 20 nA beam current. The U–Pb isotopes (^{206}Pb, ^{207}Pb, ^{208}Pb,^{232}Th and ^{238}U) and trace elements (^{49}Ti, ^{91}Zr, ^{93}Nb, ^{181}Ta and rare earth elements (REEs) analyses were conducted by a laser ablation–inductively coupled plasma–mass spectrometer (LA–ICP–MS) in the SKLMDR. Coherent Geolas Pro 193 nm laser ablation system and Thermal iCAP RQ inductively coupled plasma mass spectrometry (ICP–MS) were connected for the in situ dating, with a laser beam diameter of 32 μm. The zircon STDGJ (600 Ma, Jackson et al., 2004) was used as an external standard to correct mass bias of the ICP–MS and residual elemental fractionation. Mud Tank zircon (735 Ma) was analyzed to observe the stability and reproducibility of the instrument. NIST 610 and ^{91}Zr were used as external and internal standards for quantitative calculation of trace elements in all zircons. The experimental data were processed by GLITTER (Van Achterbergh et al., 2001). The concordia diagrams and weighted mean calculations were obtained using Isoplot (ver 3.70) (Ludwig, 2008).

ZIRCON PETROGRAPHY

Two types of zircon can be identified in the BST pluton. Type–I zircons are mainly distributed in the lower zone (zone–a) of the pluton embedded in K-feldspar and the amount of type–I zircons gradually decreases upwards (**Figure 4A**). They are transparent, colorless, prismatic and euhedral under the optical microscope (**Figure 4D**), exhibiting clear oscillatory zoning in CL images (**Figure 5A**). These zircon grains are generally 100–200 μm in size, with length–width ratios of 3:1–6:1. BSE images show that type–I zircons are dark in color and show growth zoning (**Figure 6A**). The observation of distinctive alteration textures with pores and microcracks, as well as the occurrence of fluorite inclusions, show that deuteric hydrorhermal overprinting (H.O. for short) occurs along the boundary of type–I zircon grains (**Figure 6A**) or restrictedly replace the growth zoning and core (**Figures 5B**, **6B**).

Type–II zircons are found in the samples from upper zones (zone–c to zone–e) of the BST pluton, and are mainly in contact with or interstitial to late magmatic K-feldspar, albite and zinnwaldite grains (**Figures 4B,C**), and the content of the type–II zircons increases gradually from zone–c (10–20%) to zone–e (70–80%). They are dark brown, translucent, dirty and subhedral to anhedral under the optical microscope (**Figure 4D**). Type–II zircon grains are generally 150–300 μm in length, with length–width ratios of 2:1–3:1. They are generally characterized by extremely dark, porous, microcracks–rich and inhomogeneous structures in CL images (**Figure 5C**). Numerous mineral inclusions, including fluorite (Fl) and columbite–group minerals (CGM), in voids and microcracks were observed in these zircons (**Figure 6C**). Type–II zircons with an inhomogeneous internal structure, can be subdivided into two domains in BSE images (**Figure 6D**). The light domains (LD) show a flat and smooth zircon surface. The dark domains (DD) show a rough surface and a veinlet–disseminated structure. It is noticed that some zircons show core–rim structure with the H.O. type–I zircon core and the overgrowth of type–II zircon (**Figures 4D**, **5D**).

RESULTS

Zircon U–Pb Ages

Seven groups of zircon samples from five lithological zones of the BST pluton are used for U–Pb dating, and the results are presented in **Supplementary Appendix Table 3**.

Two zircon samples from zone–a (19KH–231 and BST–27) are type–I zircon. They have Th contents of 117–2020 ppm, with a mean of 787 ppm, and U contents of 239–2,202 ppm, with a mean of 928 ppm. The Th/U ratios vary from 0.33 to 1.37. Analyses of sample 19KH–231 give closely concordant ages and all the analyzed spots fall on the concordia, yielding a weighted mean age of 250 ± 2.5 Ma (n = 9, MSWD = 0.082, 1 σ) (**Figure 7A**). Analyses of sample BST–27 are mostly concordant and fall on the concordia. Except for five discordant spots (No. BST–27–22 to –26), the remaining concordant analyses yield a weighted mean age of 250.5 ± 1.7 Ma (n = 21, MSWD = 0.35, 1 σ) (**Figure 7B**).

Zircons from zone–b (19KH–235) mainly belong to type–I zircon. They have low Th (157–2,487 ppm) and U (297–2,812 ppm) contents, with Th/U ratios of 0.40–1.39. All of the analyses deviate from the concordia, and fifteen analyses

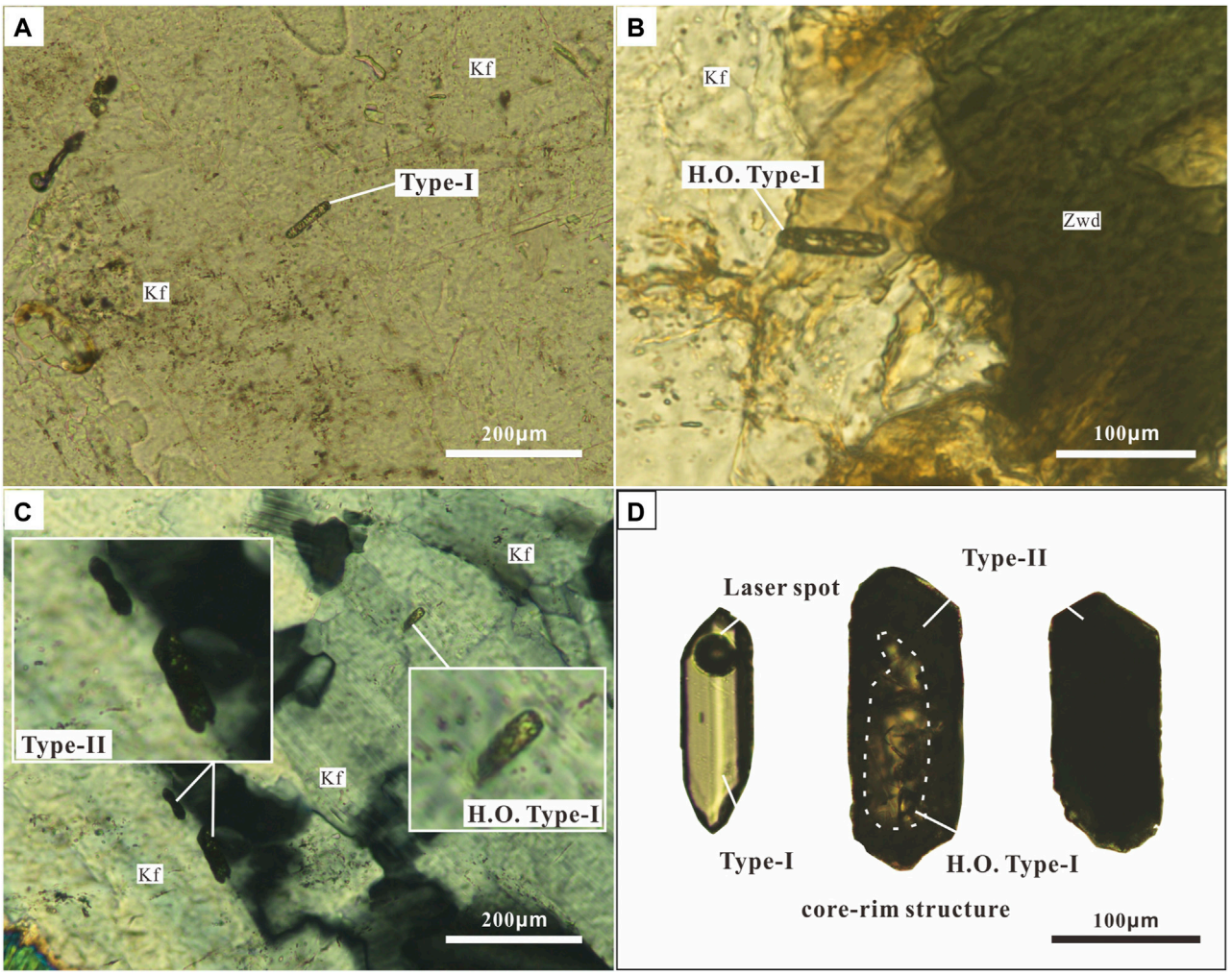

FIGURE 4 | Transmitted–light microscopic images of zircons from the BST pluton. H.O. type-I–hydrothermal overprinting type–I zircon. **(A)** Type–I zircon embedded in the K-feldspar crystal. Single polarizer. **(B)** H.O. type–I zircon contact with zinnwaldite. Single polarizer. **(C)** H.O. type–I zircon embedded in the K-feldspar and the type–II zircons contact with K-feldspar. Crossed polarizers. **(D)** Photomicrographs showing the feature of different types of zircons. The black circle in the type–I zircon is the laser spot. Single polarizer.

yield a lower intercept age of 248 ± 3.1 Ma (n = 15, MSWD = 0.18, 1 σ) (**Figure 7C**). These results indicate that there was radiogenic Pb loss probably due to metamictization of these zircons (Nasdala et al., 1996).

Fourteen analyses were conducted on the zircons from zone–c (19KH–238), including twelve type–I zircons and two xenocrysts (according to the Miller et al., 2007). The type–I zircons show variable Th (78–4,857 ppm) and U (165–3,301 ppm) contents, with Th/U ratios of 0.29–1.48. The two xenocrysts have Th contents of 294–313 ppm, U contents of 375–698 ppm and Th/U ratios of 0.45–0.78. These xenocrysts show apparent $^{238}U/^{206}Pb$ ages of 297 Ma and 441 Ma, respectively. Notably, the apparent $^{238}U/^{206}Pb$ ages of 297 Ma is consistent with the previous zircon U–Pb age obtained from zone–c (Liu et al., 2008). All analyses of the type–I zircons deviate from concordia, yielding a well–defined lower intercept age of 255 ± 10 Ma (n = 12, MSWD = 3.4, 1 σ) (**Figure 7D**).

Sixteen analyses were obtained from the zircons from zone–d (19KH–253), including eight type–I zircons, four type–II zircons, and four xenocrysts. The Th (260–1,237 ppm) and U (457–4,666 ppm) contents of type–I zircons are much lower than those of the type–II, which have Th and U contents of 1,138–4,976 ppm and 3,542–32,901 ppm, respectively. The xenocrysts have Th contents of 187–1,032 ppm, U contents of 254–1,247 ppm, and Th/U ratios of 0.61–0.83. Except for the xenocrysts and one analysis of type–II zircons, zircons from zone–d yield a lower intercept age of 238 ± 5.9 Ma (n = 11, MSWD = 0.36, 1 σ). Two analyses of type–I zircons (No. 19KH–253–01 and –07) give concordant ages of 242 ± 4 Ma and 239 ± 7 Ma, respectively (**Figure 7E**). Remarkably, the xenocrysts from the zone–d show concordant apparent $^{238}U/^{206}Pb$ ages of 298–299 Ma (**Figure 7E**), which are also consistent with previous zircon U–Pb ages (Liu et al., 2008).

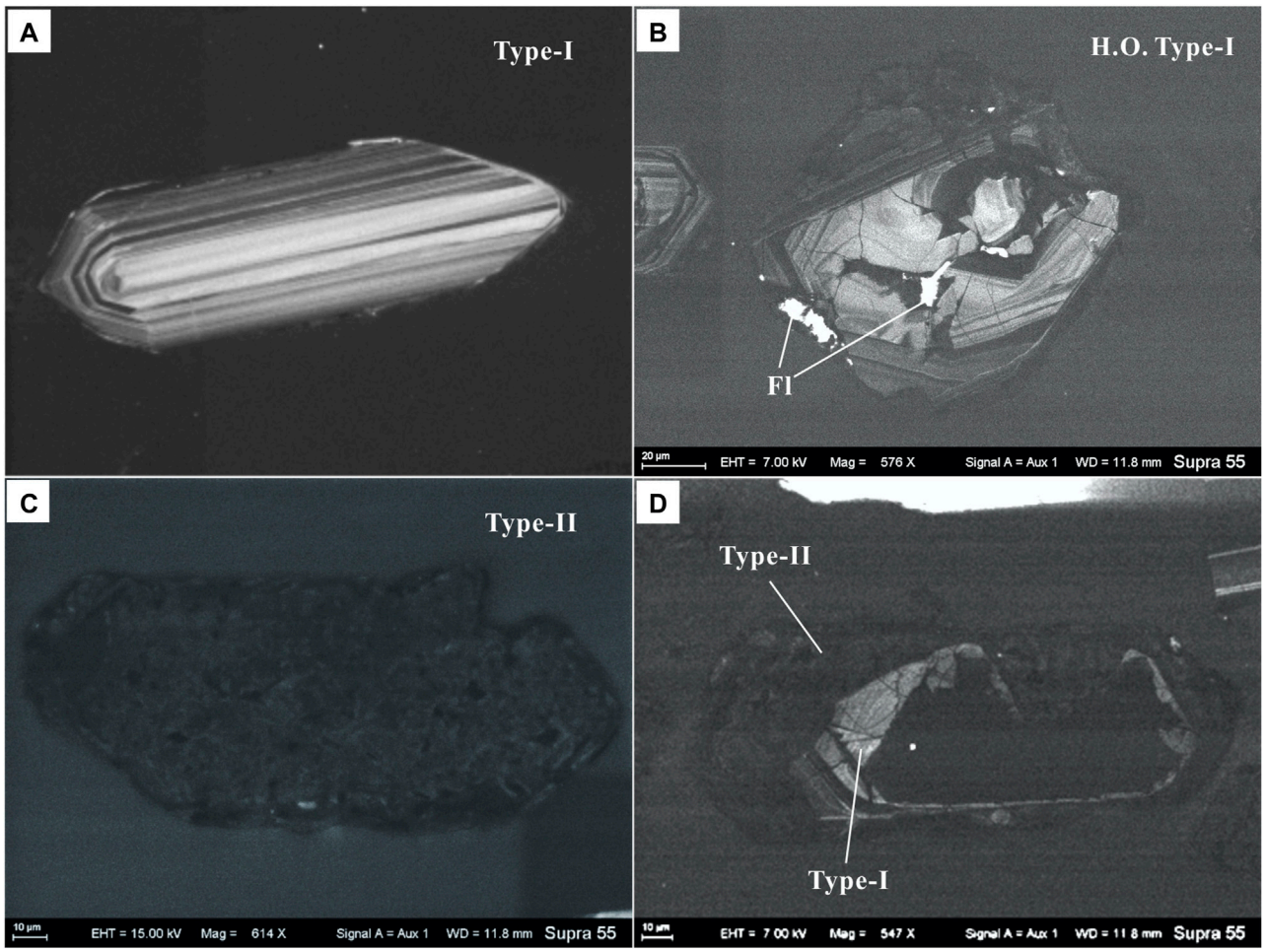

FIGURE 5 | Cathodoluminescence (CL) images of zircons from the BST pluton. **(A)** Type–I zircon with oscillatory zoning. **(B)** Type–I zircon with the hydrothermal overprinting. Fluorite inclusion occur in the microcracks of the H.O. type–I zircon. **(C)** Subhedral, dark and inhomogeneous type–II zircon grain. **(D)** Zircon grains with core–rim structure. H.O. type–I zircon in core and type–II zircon in edge.

Zircons were separated from two samples (19KH–250 and xxx–22) in zone–e. Eight analyses obtained from the 19KH–250 zircons are type–I zircon. The Th and U contents of these type–I zircons are range from 103 to 1,485 ppm and 145 to 2,182 ppm, respectively, with Th/U ratios of 0.54–1.82. They define a lower intercept age of 254 ± 13 Ma (n = 8, 1 σ, MSWD = 0.026) with a collinear array (**Figure 7F**). Forty four analyses were conducted on the zircons of sample xxx–22 (**Figure 7G**), including thirteen type–I zircons, twenty four type–II zircons and six xenocrysts. The type–I zircon show variable Th (339–3,317 ppm) and U (516–3,688 ppm) contents, with Th/U ratios of 0.17–3.29. The type–II zircons show extremely inhomogeneous concentrations of Th (386–15,943 ppm) and U (1,485–12,380 ppm), with Th/U ratios of 0.13–5.68. The xenocrysts have Th, U contents and Th/U ratios of 112–1,385 ppm, 178–1761 ppm and 0.16–0.79, respectively. Except for the xenocrysts, xxx–22 zircons yield a lower intercept age of 256.5 ± 8.0 Ma (n = 38, 1 σ, MSWD = 4.5), with all the analyses deviating from the concordia (**Figure 7H**).

Type–I zircons from zone–a (19KH–231 and BST–27) in the BST pluton show weighted average ages of 250 ± 2.5 Ma and 250.5 ± 1.7 Ma, respectively, indicating that the BST pluton was intruded in the Early Triassic. The lower intercept ages of type–I zircons from 19KH-235 (zone–b), 19KH–238 (zone–c) and 19KH–250 (zone–e) are also ca. 250 Ma. Type–II zircons from 19KH-253 (zone–d) and xxx–22 (zone–e) together with coexisting type–I zircons define the lower intercept ages (238–257 Ma), which may represent an approximate crystallization age of the type–II zircons.

Chemical Composition of the Zircons

In situ LA–ICP–MS data for trace elements in zircons are listed in **Supplementary Appendix Table 4**. Type–I zircons from the BST pluton generally have high Zr contents between 350,744 and 498,235 ppm (≈47.4–67.3 wt% ZrO_2, with a mean of 61.12 wt% ZrO_2), and low Ti (1.72–69 ppm with a mean of 9.42 ppm), Y (498–6,510 ppm with a mean of 2,184 ppm), Nb (1.19–1,470 ppm with a mean of 125 ppm), Ta (0.621–219 ppm with a mean of

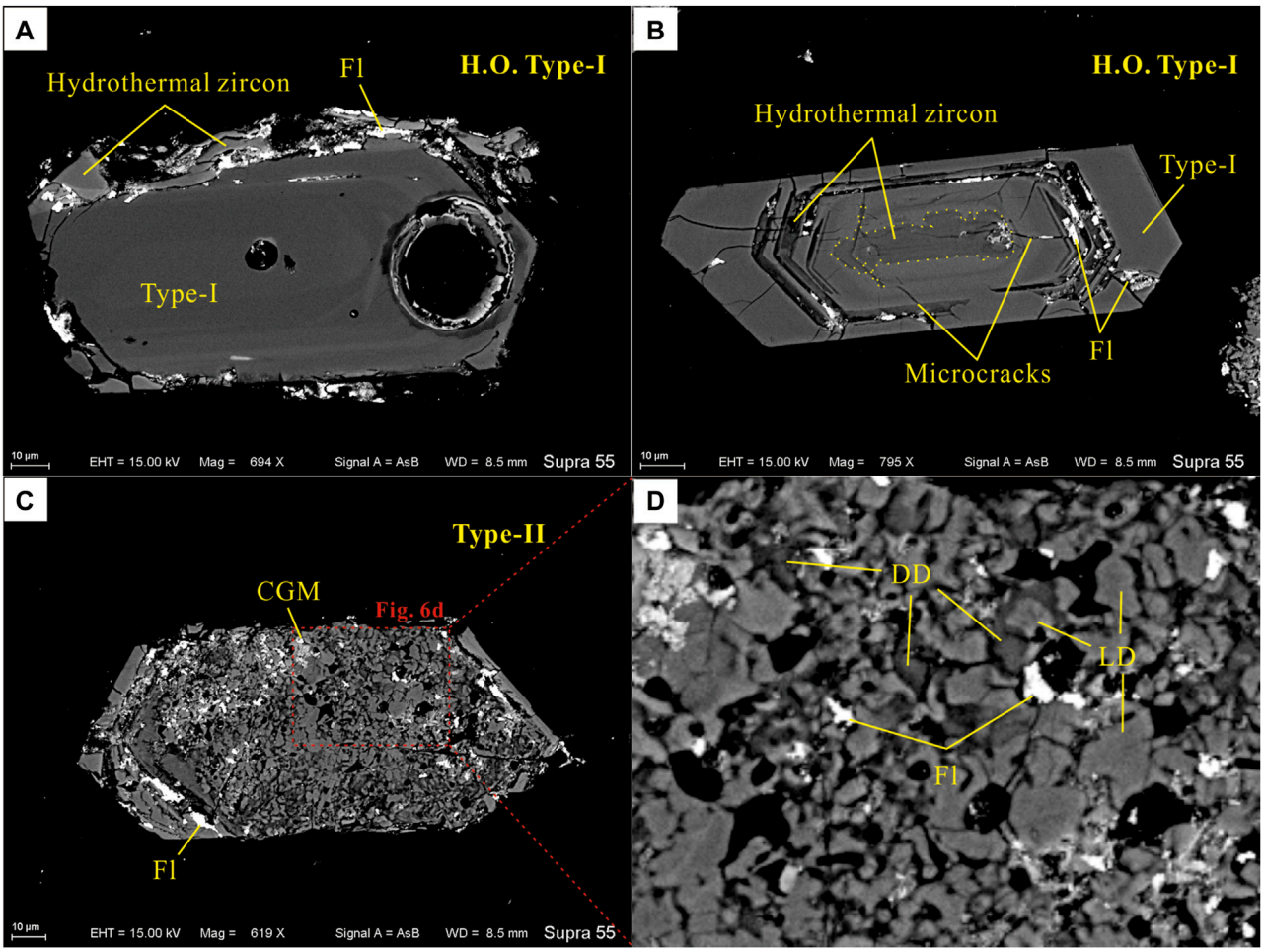

FIGURE 6 | Backscattered electron (BSE) images of zircons from the BST pluton. Fl–fluorite, CGM–columbite group minerals. **(A)** Hydrothermal zircon and fluorite occur around the type–I zircon crystal. The circle is the laser spot. **(B)** F–rich hydrothermal alteration occurs along the growth zoning and fractures in inner zone of the type–I zircon. Microcracks in the H.O. type–I zircon are partially filled with fluorite. **(C)** Type–II zircons, with a complex internal structure, contain large amount of fluorite (Fl) and columbite group mineral (CGM) inclusions in their crystals. **(D)** Closeup of the type–II zircon with the light domains (LD) and dark domains (DD). The fluorite (Fl) inclusions are embedded in microcraks and voids in type–II zircon.

12.99), Hf (7,471–20,835 ppm with a mean of 11,269 ppm), Th (78.2–2,810 ppm with a mean of 770 ppm and a median of 442 ppm), and U (165–2,810 ppm with a mean of 897 ppm and a median of 630 ppm) concentrations, as well as minor amounts of the light REE (LREE) (27–604 ppm with a mean of 110 ppm), heavy REE (HREE) (388–4,029 ppm with a mean of 1,512 ppm) corresponding to total REE of 451–4,590 ppm with a mean of 1,679 ppm. They show HREE–enriched patterns with prominent positive Ce anomalies ($Ce/Ce^* = 1.21–385$), strong negative Eu anomalies ($Eu/Eu^* = 0.008–0.551$) and low LREE/HREE ratios (0.04–0.26 with a mean of 0.10) (**Figures 8A–E**). They have Zr/Hf ratios ranging from 21.72 to 58.23 with a mean of 41.48 (**Figure 8F**) and Th/U ratios from 0.29 to 2.08 with a mean of 0.84 (**Figure 9A**).

Type–II zircons vary greatly in chemical composition and are enriched in trace elements. They have low Zr contents of 286,445–377627 ppm (≈38.7–51.0 wt% ZrO_2 with a mean of 47.45 wt% ZrO_2), and unusually high contents of Hf (34,094–85,754 ppm with a mean of 67,983 ppm), Y (1,630–28,890 ppm with a mean of 8,434 ppm), Nb (171–2,520 ppm with a mean of 1,216 ppm), Ta (86.7–398 ppm with a mean of 167 ppm), Th (718–4,980 ppm with a mean of 2,136 ppm and a median of 1730 ppm) and U (3,540–32,901 ppm with a mean of 7,898 ppm and a median of 5,440 ppm). The concentrations of Ti (0–42.6 ppm with a mean of 12.44 ppm) are similar to those of the type–I. They have Zr/Hf ratios ranging from 3.35 to 11.00 with a mean of 5.56 (**Figure 8F**) and Th/U ratios from 0.12 to 0.57 with a mean of 0.36 (**Figure 9A**). The LREE, HREE, total REE contents and LREE/HREE ratios vary from 267 to 6,523 ppm with a mean of 2095 ppm, 3,628–23,640 ppm with a mean of 9,670 ppm, 3,909–30,163 ppm with a mean of 11,765 ppm, and 0.07–0.35 with a mean of 0.20, respectively, which are much higher than those of type–I zircon (**Figure 9B**).

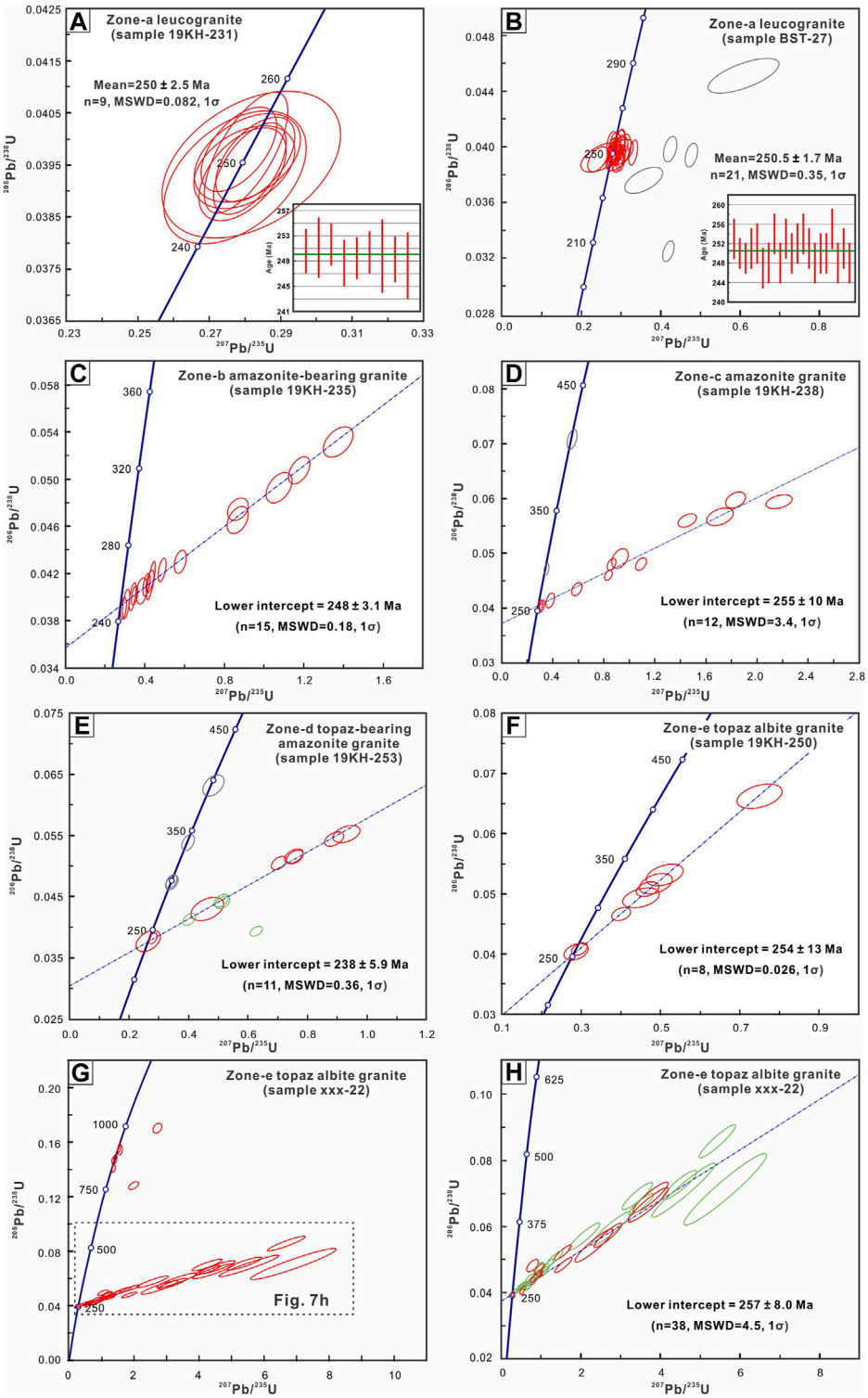

FIGURE 7 | (A,B) U–Pb concordia diagrams and weighted average ages of type–I zircon from zone–a. **(C–H)** U–Pb concordia diagrams of type–I (red circle) and type–II (green circle) zircons from the upper zones of the BST pluton.

Type–II zircons exhibit gull wing–shaped, slightly HREE–enriched patterns with lower positive Ce anomalies (Ce/Ce^{*} = 2.1–10.3) and deeper Eu anomalies (Eu/Eu^{*} = 0–0.006) than those of the type–I zircons (**Figure 9C**). Chondrite–normalized REE patterns of type–II zircons display clearer tetrad effect than the type–I. The t_3 value

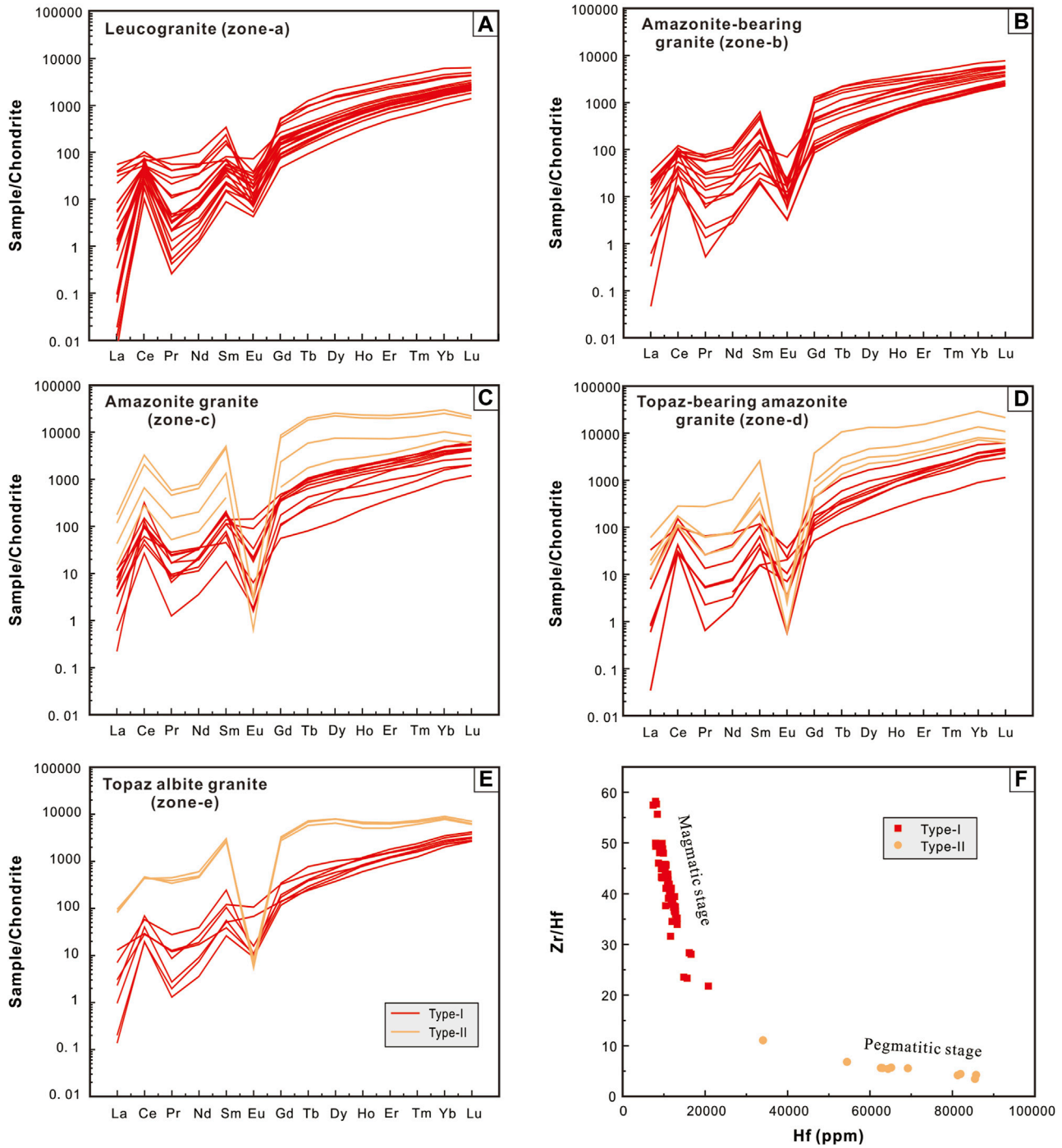

FIGURE 8 | (A–E) Chondrite–normalized REE distribution patterns and **(F)** Zr–Hf fractionation trends for two types of zircon from the each zones of the BST pluton. Values for magmatic stage and pegmatitic stage are from Wang et al. (2010) and Han et al. (2019) and reference therein.

(quantification factor of tetrad effect) and ∑HREE can be used to describe the tetrad effect of the zircons, and is calculated and listed in **Supplementary Appendix Table 4**. The t_3 value in zircons from the BST pluton are generally greater than 1. The t_3 values of both two types of zircons have strongly positive correlation with ∑HREE (**Figure 9D**), and increases from type–I zircons (0.89–1.46) to type–II zircons (1.51–1.69).

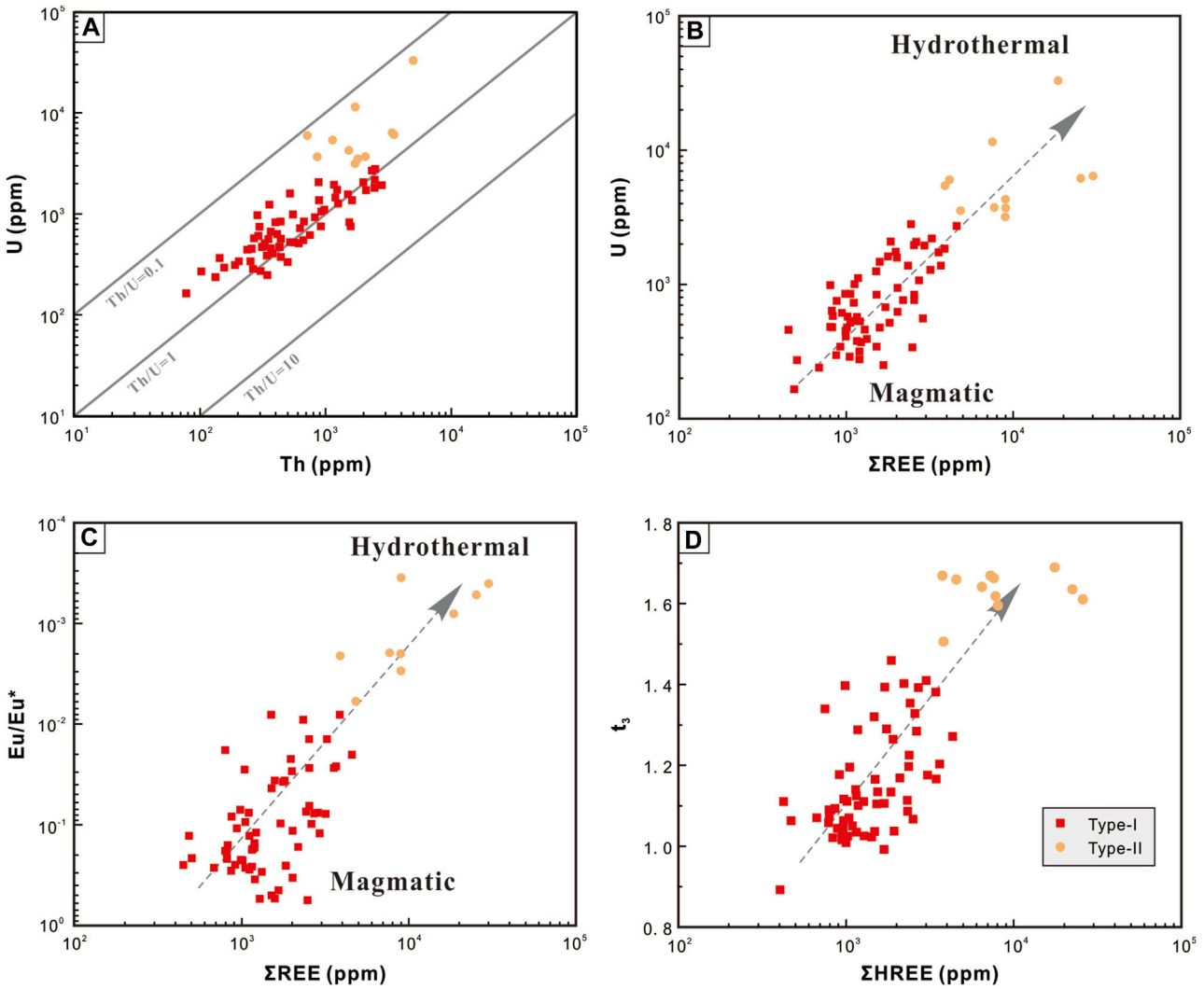

FIGURE 9 | Plots of **(A)** U vs. Th, **(B)** U vs. ∑REE, **(C)** Eu/Eu* vs. ∑REE, and **(D)** comparison of quantification factor t_3 to ∑HREE of two types of zircon from the BST pluton. All data come from **Supplementary Appendix Table 4**.

DISCUSSION

Zircon Genesis

The zircons in the BST pluton can be divided into two types: type–I and type–II, based on their distinct petrographic features, crystal structures and chemical compositions.

Type–I zircons are clean, transparent, colorless and euhedral under the optical microscope (**Figure 4D**), and are bright and show clear oscillatory zoning in CL (**Figure 5A**), consistent with a magmatic origin (Corfu et al., 2003). They are primarily distributed at the bottom of the granite (zone–a), and embedded in K-feldspar crystals (**Figure 4A**), indicating that they crystallized before K-feldspar. Chemically, the type–I zircons are characterized by high Zr and low trace element contents. They show HREE–enriched patterns with prominent positive Ce anomalies (Ce/Ce* = 1.21–385) and strong negative Eu anomalies (Eu/Eu* = 0.008–0.551). The contents of LREE vary from 27 to 604 ppm and HREE from 403 to 4,320 ppm with LREE/HREE ratios of 0.04–0.26. The low concentrations of Th, U and high Th/U ratios (mostly >0.4) are comparable to those of zircons crystallized in early magmatic stages (U contents of 76–12,381 ppm with a median of 764 ppm and Th contents of 31–12,088 ppm with a median of 368 ppm, Belousova et al., 2002; UO_2 contents of 0–0.56 wt% (≈0–4,936 ppm U) with an average of 0.30 wt% (≈2,644 ppm U) and ThO_2 contents of 0–0.15 wt% (≈0–1,318 ppm Th) with an average of 0.04 wt% (≈352 ppm Th), Wang et al., 2011). The Hf contents of 7,471–20,835 ppm, with an average of 11,269 ppm (≈1.33 wt% HfO_2), and Zr/Hf ratios of 22–58 are consistent with primary granitic zircons crystallized at high temperature (<2 wt% HfO_2 and Zr/Hf > 27, Pupin et al., 2000; model HfO_2 contents of 1.43 wt% and Zr/Hf ratios of 38.5, Wang et al., 2010). Gu et al. (2003) indicate that the

homogenization temperatures of melt trapped in quartz phenocrysts decrease from the zone–a (810–860°C) to the zone–e (680–660°C) in the BST pluton. Type–I zircons are mainly distributed in the zone-a. Therefore, they are considered to be high temperature magmatic zircons.

Type–II zircons are dark brown, translucent, dirty and euhedral to subhedral under the optical microscope, and are porous, microcracks–rich and inhomogeneous in structures in CL and BSE images, consistent with the petrographic features of hydrothermal zircons (e.g., Wang et al., 2011, Wang X. et al., 2016, Wang and Ren, 2018). The contents of Hf, Nb, Ta, Y, Th, U, LREE and total REE in type–II zircons are much higher than in type–I. They show slightly HREE–enriched patterns with lower positive Ce anomalies (Ce/Ce^* = 2.1–10.3) and deeper Eu anomalies (Eu/Eu^* = 0–0.006) than those of the type–I zircons. The high LREE and HREE contents and LREE/HREE ratios of type-II zircons are consistent with a hydrothermal origin (LREE contents of 608–2,502 ppm with a mean of 1,303 ppm, HREE contents of 324–4,990 ppm with a mean of 2064 ppm, and LREE/HREE ratios of 0.29–5.49 with a mean of 1.20, Yang et al., 2014). The generally higher Th (718–4,980 ppm with a mean of 2,136 ppm), U (3,180–32,901 ppm with a mean of 7,898 ppm) contents and lower Th/U ratios (mostly <0.4, **Figure 9A**) of type–II zircons are comparable to those of zircons of hydrothermal origin in highly evolved magmatic systems (U contents of 560–3,820 ppm with a mean of 1710 ppm, Th contents of 83.0–12,638 ppm with a mean of 1,594 ppm, and Th/U ratios of 0.11–0.54, Yang et al., 2014). The extremely high Hf contents (up to 10.1 wt% Hf_2O) and low Zr/Hf ratios of type–II zircons in the BST pluton (**Figure 6F**) are also comparable to zircons from the pegmatite or highly evolved granite (>2.4wt% HfO_2 and Zr/Hf ratios ≤20, Gbelsky, 1979; Cerny et al., 1985). The much higher Hf contents and low Zr/Hf ratios of zircons from granitic rocks (especially hydrothermal zircons) could be caused by low crystallization temperatures (Wang et al., 2010, Wang X. et al., 2016). Moreover, the positive relationship between U and ∑REE (**Figure 9B**), and the increase of negative Eu anomalies from type–I to type–II zircons (**Figure 9C**), suggest the increase of hydrothermal contribution to zircon crystallization (Veksler, 2004; Hoskin, 2005). Thus, type–II zircons from the BST pluton are interpreted to be of hydrothermal origin.

The high contents of LREE and low Zr/Hf ratios in type–II zircon could be the result of non–charge–and–radius–controlled (Non–CHARAC) behavior (Bau and Dulski, 1995; Bau, 1996), which commonly occurs in volatile–rich highly evolved magmatic systems during the transition from magmatic to hydrothermal conditions (Veksler, 2004). Non–CHARAC behavior is often accompanied by the lanthanide tetrad effect of both whole–rock and minerals including zircon (Masuda and Ikeuchi, 1979; Akagi et al., 1993; Bau, 1996; Irber, 1999; Veksler et al., 2005). Type–II zircons in the BST pluton show obvious M–type tetrad patterns in chondrite–normalized REE distribution patterns with t_3 values of 1.51–1.69, consistent with the clear tetrad features of other minerals in the BST pluton, such as quartz, plagioclase, garnet and monazite (Wu et al., 2011). The lanthanide tetrad effect is generally attributed to hydrothermal fluid–rock interaction (Monecke et al., 2002; Monecke et al., 2007; Takahashi et al., 2002; Badanina et al., 2006), and the M–type tetrad patterns are considered to be caused by F–rich magmatic fluid–melt interaction above the solidus (Wu et al., 2011). Thus, the formation of type–II zircons should represent a magmatic fluid–melt interaction during the transition from magmatic to F–rich hydrothermal conditions. At this stage, Th, U, Hf, Ta, REEs and other trace elements in the magmatic system were significantly concentrated in the magmatic fluids that coexisted with the melt.

F–Rich Fluid Exsolution and Magmatic–Hydrothermal Transition

The Rb-bearing granites in the Eastern Tianshan are characterized by high SiO_2, Na_2O, K_2O Li, Rb, Cs and F, low Ti, Fe, Ca, Mg and P, $Na_2O > K_2O$, are weakly peraluminous (A/NKC = 1.00–1.11), low K/Rb, Al/Ga, Y/Ho, Zr/Hf and Nb/Ta ratios, and have low $(La/Lu)_N$ and deep Eu anomalies (Gu et al., 2003; Chen et al., 2018; Li T. G. et al., 2018; Muhtar et al., 2020a). They are generally highly evolved magmatic systems with abundant deuteric fluid exsolution and hydrothermal alteration occurring in the late magmatic stage. A previous study has suggested that several fluid exsolution events occurred during the differentiation of magma, controlling the formation and modification of the highly evolved granite (Berni et al., 2017; Berni et al., 2020).

The present study observed that ∑HREE and t_3 values show linear variations between two types of zircon, with t_3 values increasing markedly from type–I to type–II zircons (**Figure 9D**). Such a trend of evolution may represent the increase of F–rich fluid–melt interaction during the differentiation of F–Rb–rich granitic magma (Wu et al., 2011). However, ∑HREE and t_3 values of zircons from zone–a to zone–e do not show linear variations, and the two types of zircons of different origin occur together in the upper lithological zones. A possible explanation is that turbulence in the volatile (F) –rich magmatic–hydrothermal system disturbed the original distribution of zircons (Gu et al., 2011), and the type–I zircons were carried to the top of the granite contained by late magmatic minerals. Moreover, modification of crystallized rocks and zircons by exsolved (F–rich) fluids occurs in the BST pluton, evidenced by large amounts of fluorite in the microcracks in magmatic type–I zircons (**Figure 6B**) and in voids of some hydrothermal type–II zircons (**Figure 6D**). The hydrothermal fluorite occurs as a vein along plagioclase, K-feldspar and zinnwaldite grains and fractures (Gu et al., 2011), also indicating the existence of a F–rich hydrothermal event after the crystallization of rock–forming minerals.

Both zircon types can be found in the same grain (**Figure 5D**), which is crucial to study the F–rich fluid exsolution processes, including F–rich fluid–melt interaction and hydrothermal modification, during the magmatic–hydrothermal transition stage. The petrography observations and geochemical compositions of zircons suggest that type–I zircons crystallized earlier than type–II zircons. Some type–I zircons crystallized in the early–magmatic stage were modified by the F–rich fluids

through dissolution–reprecipitation at the edges (**Figure 6A**) or along defective magmatic euhedral zones (**Figure 6B**), consistent with petrographic features of hydrothermal overprinting of zircons (e.g., Wang and Ren, 2018; Liu et al., 2019, Han et al., 2019). This supports the mobilization of Zr in hydrothermal systems that are rich in F (Rubin et al., 1993; Aja et al. 1995; Veksler et al., 2005). Such selective alteration of zircon grains probably occurs as a result of metamictization (e.g., Geisler et al., 2007; Van Lichtervelde et al., 2009; Liu et al., 2019). Radiation–induced metamictization can greatly enhance (two or three times compared to high crystallinity zircons) the hydrothermal alteration of zircons (Ewing et al., 2003). The alpha recoil process (i.e., recoils of the U and Th nuclei after emitting a He particle) can be a main source of damage in metamictization (Wasilewski et al., 1973; Smith et al., 1991; Weber et al., 1994; Nasdala et al., 1996, 2001; Palenick et al., 2003), which can accumulate rapidly over a period of 0.0001–1 million years in the zircon grains. Then, the deuteric F–rich fluid locally replaced some type–I zircons, from which the hydrothermal type–II zircon and fluorite crystallized as overgrowth of the type–I (**Figures 4D**, **5D**). Gradual increase of the amount of the hydrothermal type–II zircons upward within the zoned granite (increase from 10 to 20% in zone–c to 70–80% in zone–e), as well as the intense modification of zircon in zone–e, suggest that a F–rich fluid could rise and accumulate to form a segregated fluid phase at the top of the BST magma (Burnham, 1997; Wilkinson, 2001; Gu et al., 2011), which is comparable to the magmatic to hydrothermal evolution in other highly evolved granites (e.g.,Yang et al., 2014; Berni et al., 2020).

Previous studies suggested that the source of the BST magma is mica gneiss in the middle crust, partial melting of which can provide large amounts of F, Rb and Cs, based on the high Na_2O + K_2O, low FeO, MgO and TiO_2 contents, the weakly peraluminous character, low εNd(t) value and $\delta^{18}O$ value (9.25–9.75 in zone-a) (Gu et al., 2011). The Rb is transported in the form of complex with F in highly evolved granitic magma (Hildreth, 1981; Jia, 2016), and the hydrolysis takes place with the decrease of temperature (Webster and Holloway, 1990; Zhao et al., 2008). The homogenization temperatures of melt trapped in quartz phenocrysts and the petrographic studies suggest that the mineral composition of the zone-a can approximately represent the mineral assemblages of the early magmatic stage (Gu et al., 2003). At this stage, F tends to enter the fluid phase and form stable complexes with Li, Rb, Cs, Sn and other elements (Hildreth, 1981; Cerny et al., 1985; Bhalla et al., 2005; Sun, 2013; Jia, 2016). With the decrease of temperature hydrolysis takes place (Webster and Holloway, 1990; Zhao et al., 2008), the $F^-$and Ca^{2+} form fluorite, and Rb replaces part of the K into the lattice of the low temperature microcline and zinnwaldite, consistent with the observation of the enrichment of Rb in low temperature K-feldspar (microcline) and mica (zinnwaldite) in the highly evolved granite (e.g., Wang et al., 2009; Badanina et al., 2010; Seltmann et al., 2010; Tang and Zhang, 2015; Ostrooumov, 2015; Li T. G. et al., 2018). The coupling of F and Rb in the early magmatic stage is also consistent with the positive correlation between Rb and F from zone-a to zone-d in the BST pluton (Gu et al., 2003, 2011). Magmatic fluid from F–rich highly evolved granite and related pegmatite contains high concentrations of trace elements including Rb (Berni et al., 2020), and the ore minerals (e.g., amazonite and zinnwaldite) in the BST pluton generally crystallized from residual magma that has experienced the F–fluid exsolution during the magmatic–hydrothermal transition (Gu et al., 2003; Gu et al., 2011), indicating that the enrichment and mineralization of Rb is closely related to the magmatic F–rich fluids.

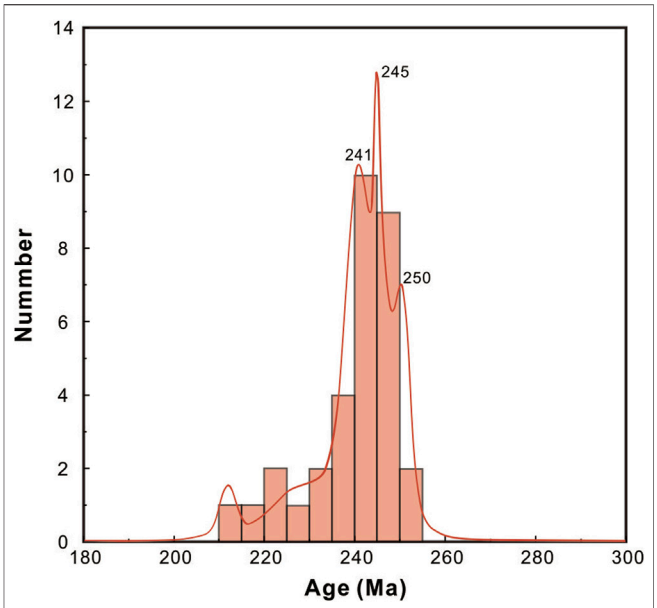

FIGURE 10 | Age data histogram of the Triassic granitic intrusions and related rare metal deposits from the Eastern Tianshan.

Therefore, F–rich fluid exsolution during the magmatic-hydrothermal transitional stage is one of the important factors controlling the modification of highly evolved granites (Gu et al., 2011; Berni et al., 2017; Berni et al., 2020), as well as related Rb enrichment and mineralization.

Implication for Rb Mineralization Age of the Zhangbaoshan Super–Large Rb Deposit

The LA–ICP–MS U–Pb data for type–I zircons from the leucogranite (zone–a) show a concordant age of 250.5 ± 1.7 Ma and 250 ± 2.5 Ma (**Figures 7A**,**B**), indicating that the BST pluton was emplaced in the Early Triassic. Type–II zircons from zone–c to zone–e show lead loss on the U–Pb concordia diagrams, yielding lower intercept U–Pb ages between 238 and 257 Ma (**Figures 7E–H**), which could indicate the age of the F–rich fluid–melt interaction above solidus during the transition from magmatic to hydrothermal conditions. These Early Triassic ages are also consistent with the emplacement age of the BST granitic magma.

As discussed above, the rubidium mineralization of the ZBS super–large Rb deposit mainly occurred during the magmatic–hydrothermal transition stage, which was later than the crystallization of magmatic type-I zircon, and close to the

crystallization age of the hydrothermal type–II zircon. We thus suppose that the rubidium mineralization occurred shortly after the emplacement age (ca. 250 Ma) of the BST pluton.

Triassic granitoids and related rare metal deposits have been increasingly identified in the Eastern Tianshan during the past decade (**Supplementary Appendix Table 1** and **Figure 10**). The ZBS granite–type super–large Rb deposit (ca. 250 Ma) and other rare–metal granite or pegmatite deposits in the Eastern Tianshan, including the Shadong W–(Rb) deposit (239 ± 2 Ma, Chen et al., 2018), the Guobaoshan Rb deposit (240.3 ± 1.8 Ma, Li T. G. et al., 2018) and the Jing'erquanbei (Li–Be–Rb) pegmatite (250.2 ± 3.5 Ma, Muhtar et al., 2020a), likely make up a >200–km–long rare metal metallogenic belt. A summary of the rare metal deposits in the Eastern Tianshan suggests that the Triassic should be an important rare metal metallogenic period in the Eastern Tianshan, and rare metal deposits are closely related to the Triassic highly evolved leucogranite enriched in F in the Eastern Tianshan.

CONCLUSION

1) Zircon from the BST pluton can be divided into two genetic types. Type–I zircons are early magmatic zircons, characterized by clear oscillatory zoning, high Zr contents and Zr/Hf ratios, low trace element concentrations, and HREE–enriched patterns. Type–II zircons are hydrothermal zircons crystallized from deuteric F–rich fluid that coexisted with residual magma. They are characterized by low Zr contents and Zr/Hf ratios, high Hf, Th, U, Ta, Y and REEs concentrations, and significant M–type tetrad patterns in chondrite–normalized REE distribution patterns.
2) The formation of type–II zircons represents a magmatic fluid–melt interaction during the transition from the magmatic to the F–rich hydrothermal stage of the BST pluton. The F–rich fluid exsolution during the magmatic–hydrothermal transition is one of the important factors controlling the modification of highly evolved granite and related Rb enrichment and mineralization.
3) Type–I zircons from leucogranite (zone–a) show a concordant age of ca. 250 Ma, indicating that the BST pluton was emplaced in the Early Triassic. Type–II zircons from zone–c to zone–e yield lower intercept U–Pb ages between 238 and 257 Ma, which could indicate the age of the F–rich fluid–melt interaction during the transition stage from the magmatic to the hydrothermal conditions. The mineralization of the ZBS super–large Rb deposit should occur shortly after emplacement of the BST pluton in the Early Triassic.
4) The Triassic should be an important rare metal metallogenic period of the Eastern Tianshan. The rare metal mineralization are closely related to the Triassic highly evolved F–rich leucogranite in the Eastern Tianshan.

DATA AVAILABILITY STATEMENT

The original contributions presented in the study are included in the article/**Supplementary Material**, further inquiries can be directed to the corresponding author.

AUTHOR CONTRIBUTIONS

RL and CW designed the study, leaded the field investigation and revised the manuscript, JZ, BC and MM participated in field work, JZ, FZ and KZ analyzed the sample and acquired the data, YC made great contributions in explanation of experimental results. All authors contributed to the writing of the manuscript, and reviewed the manuscript and agree to this submission.

FUNDING

This study is supported by Natural Science Foundation of China (No. 91962214) and National Key R&D Program of China (Grant No. 2018YFC0603703).

ACKNOWLEDGMENTS

We thank Tongguo Li and Youkui Zhang from Geological Survey Academy of Gansu Province, and Kai Gan, Simeng Wang and Xianglong Luo from Nanjing University for their assistance in fieldwork.

SUPPLEMENTARY MATERIAL

The Supplementary Material for this article can be found online at: https://www.frontiersin.org/articles/10.3389/feart.2021.682720/full#supplementary-material

REFERENCES

Aja, S. U., Wood, S. A., and Williams-Jones, A. E. (1995). The Aqueous Geochemistry of Zr and the Solubility of Some Zr-Bearing Minerals. *Appl. Geochem.* 10 (6), 603–620. doi:10.1016/0883-2927(95)00026-7

Akagi, T., Shabani, M. B., and Masuda, A. (1993). Lanthanide Tetrad Effect in Kimuraite [CaY2(CO3)4 · 6H2O]: Implication for a New Geochemical index. *Geochimica et Cosmochimica Acta* 57 (12), 2899–2905. doi:10.1016/0016-7037(93)90397-f

Ayers, J. C., Zhang, L., Luo, Y., and Peters, T. J. (2012). Zircon Solubility in Alkaline Aqueous Fluids at Upper Crustal Conditions. *Geochimica et Cosmochimica Acta* 96, 18–28. doi:10.1016/j.gca.2012.08.027

Badanina, E. V., Syritso, L. F., Volkova, E. V., Thomas, R., and Trumbull, R. B. (2010). Composition of Li-F Granite Melt and its Evolution during the Formation of the Ore-Bearing Orlovka Massif in Eastern Transbaikalia. *Petrology* 18 (2), 131–157. doi:10.1134/s0869591110020037

Badanina, E. V., Trumbull, R. B., Dulski, P., Wiedenbeck, M., Veksler, I. V., and Syritso, L. F. (2006). The Behavior of Rare-Earth and Lithophile Trace Elements in Rare-Metal Granites: a Study of Fluorite, Melt Inclusions and Host Rocks

from the Khangilay Complex, Transbaikalia, Russia. *Can. Mineral.* 44 (3), 667–692. doi:10.2113/gscanmin.44.3.667

Bau, M. (1996). Controls on the Fractionation of Isovalent Trace Elements in Magmatic and Aqueous Systems: Evidence from Y/Ho, Zr/Hf, and Lanthanide Tetrad Effect. *Contrib. Mineralogy Petrol.* 123 (3), 323–333. doi:10.1007/s004100050159

Bau, M., and Dulski, P. (1995). Comparative Study of Yttrium and Rare-Earth Element Behaviours in Fluorine-Rich Hydrothermal Fluids. *Contrib. Mineralogy Petrol.* 119 (2–3), 213–223. doi:10.1007/s004100050037

Belousova, E. A., Griffin, W. L., and O'Reilly, S. Y. (2006). Zircon crystal Morphology, Trace Element Signatures and Hf Isotope Composition as a Tool for Petrogenetic Modelling: Examples from Eastern Australian Granitoids. *J. Petrol.* 47 (2), 329–353. doi:10.1093/petrology/egi077

Belousova, E., Griffin, W., O'Reilly, S. Y., and Fisher, N. (2002). Igneous Zircon: Trace Element Composition as an Indicator of Source Rock Type. *Contrib. Mineral. Petrol.* 143 (5), 602–622. doi:10.1007/s00410-002-0364-7

Berni, G. V., Wagner, T., and Fusswinkel, T. (2020). From a F-Rich Granite to a NYF Pegmatite: Magmatic-Hydrothermal Fluid Evolution of the Kymi Topaz Granite Stock, SE Finland. *LITHOS* 364-365, 105538. doi:10.1016/j.lithos.2020.105538

Berni, G. V., Wagner, T., Fusswinkel, T., and Wenzel, T. (2017). Magmatic-hydrothermal Evolution of the Kymi Topaz Granite Stock, SE Finland: mineral Chemistry Evidence for Episodic Fluid Exsolution. *Lithos* 292-293, 401–423. doi:10.1016/j.lithos.2017.09.015

Bhalla, P., Holtz, F., Linnen, R. L., and Behrens, H. (2005). Solubility of Cassiterite in Evolved Granitic Melts: Effect of T, fO2, and Additional Volatiles. *Lithos* 80 (1-4), 387–400. doi:10.1016/j.lithos.2004.06.014

Burnham, C. W. (1997). "Magmas and Hydrothermal Fluids," in *Geochemistry of Hydrothermal Ore Deposites*. Editor H. L. Barnes. third edition (New York: John Wiley & Sons), 63–124.

Cerny, P., Meintzer, R. E., and Andreson, A. J. (1985). Extreme Fractionation in Rare-Element Granitic Pegmatites: Selected Examples of Data and Mechanisms. *Can. Mineral.* 23, 381–421.

Chen, C., Lü, X., Wu, C., Jiang, X., and Mao, C. (2018). Origin and Geodynamic Implications of Concealed Granite in Shadong Tungsten Deposit, Xinjiang, China: Zircon U-Pb Chronology, Geochemistry, and Sr-Nd-Hf Isotope Constraint. *J. Earth Sci.* 29 (01), 114–129. doi:10.1007/s12583-017-0808-7

Chen, X., Shu, L., and Santosh, M. (2011). Late Paleozoic post-collisional Magmatism in the Eastern Tianshan Belt, Northwest China: New Insights from Geochemistry, Geochronology and Petrology of Bimodal Volcanic Rocks. *Lithos* 127 (3), 581–598. doi:10.1016/j.lithos.2011.06.008

Chen, Y. (1999). *Geochemistry of Granites from the Eastern Tianshan Mountains and the Northern Qinling Belt*. Beijing: Geological Publishing House. (in Chinese).

Chen, Y. L., and Wang, Z. G. (1993). Geochemical Characteristics of East Tianshan Granitoid Rocks, Xinjiang, China. *Geochimica* 3, 288–302. (in Chinese).

Chen, Z. H., Wang, D. H., Gong, Y. F., Chen, Y. C., and Chen, S. P. (2006). ^{40}Ar-^{39}Ar Isotope Dating of Muscovite from Jingerquan Pegmatite Rare Metal deposit in Hami, Xinjiang, and its Geological Significance. *Mineral. Deposit* 25 (4), 471–476. (in Chinese).

Chen, Z., Xiao, W., Windley, B. F., Schulmann, K., Mao, Q., Zhang, Z., et al. (2019). Composition, Provenance, and Tectonic Setting of the Southern Kangurtag Accretionary Complex in the Eastern Tianshan, NW China: Implications for the Late Paleozoic Evolution of the North Tianshan Ocean. *Tectonics* 38 (8), 2779–2802. doi:10.1029/2018tc005385

Coleman, R. G. (1989). Continental Growth of Northwest China. *Tectonics* 8 (3), 621–635. doi:10.1029/tc008i003p00621

Corfu, F., Hanchar, J. M., Hoskin, P. W. O., and Kinny, P. (2003). 16. Atlas of Zircon Textures. *Rev. Mineralogy Geochem.* 53, 469–502. doi:10.1515/9781501509322-019

Deng, X.-H., Chen, Y.-J., Santosh, M., Wang, J.-B., Li, C., Yue, S.-W., et al. (2017). U-pb Zircon, Re-os Molybdenite Geochronology and Rb-Sr Geochemistry from the Xiaobaishitou W (-Mo) Deposit: Implications for Triassic Tectonic Setting in Eastern Tianshan, NW China. *Ore Geology. Rev.* 80, 332–351. doi:10.1016/j.oregeorev.2016.05.013

Erdmann, S., Wodicka, N., Jackson, S. E., and Corrigan, D. (2013). Zircon Textures and Composition: Refractory Recorders of Magmatic Volatile Evolution?. *Contrib. Mineral. Petrol.* 165 (1), 45–71. doi:10.1007/s00410-012-0791-z

Ewing, R. C., Meldrum, A., Wang, L., Weber, W. J., and Corrales, L. R. (2003). Radiation Effects in Zircon. *Rev. Mineralogy Geochem.* 53, 378–420. doi:10.2113/0530387

Gansu Provincial Geological Survey Institute (GPGSI) (2015). Internal Reconnaissance Report of the Zhangbaoshan Ru-Polymetallic deposit in Hami City, Xinjiang Province. (Unpublished report (in Chinese).

Gbelsky, J. (1979). Electron Microprobe Determination of Zr/Hf Ratios in Zircons from Pegmatites of the Male Karpaty Mts (West Carpathians). *Geologica Carpathica* 30, 463–474.

Geisler, T., Schaltegger, U., and Tomaschek, F. (2007). Re-equilibration of Zircon in Aqueous Fluids and Melts. *Elements* 3 (1), 43–50. doi:10.2113/gselements.3.1.43

Gu, L. X., Gou, X. Q., Zhang, Z. Z., Wu, C. Z., Liao, J. J., Yang, H., et al. (2003). Geochemistry and Petrogenesis of a Multi-Zoned High Rb and F Granite in Eastern Tianshan. *Acta Petrologica Sinica* 19 (4), 585–600. (in Chinese). doi:10.3321/j.issn:1000-0569.2003.04.001

Gu, L. X., Hu, S. X., Yu, C. S., Zhao, M., Wu, C. Z., and Li, H. Y. (2001). Intrusive Activities during Compression-Extension Tectonic Conversion in the Bogda Intracontinental Orogen. *Acta Petrologica Sinica* 17 (2), 187–198. (in Chinese). doi:10.3321/j.issn:1000-0569.2001.02.002

Gu, L. X., Yang, H., Gou, X. Q., Guo, J. C., and Wang, J. Z. (1994). Geology and Genesis of the Baishitouquan High-Rubidium and Fluorine Granites in the Xingxingshia District of Hami County, Xinjiang. *Acta petrologica sinica* 10 (1), 41–53.

Gu, L. X., Zhang, Z. Z., Wu, C. Z., Wang, Y. X., Tang, J. H., Wang, C. S., et al. (2006). Some Problems on Granites and Vertical Growth of the continental Crust in the Eastern Tianshan Mountains, NW China. *Acta Petrologica Sinica* 22 (5), 1103–1120. (in Chinese). doi:10.3321/j.issn:1000-0569.2006.05.005

Gu, L.-x., Zhang, Z.-z., Wu, C.-z., Gou, X.-q., Liao, J.-j., and Yang, H. (2011). A Topaz- and Amazonite-Bearing Leucogranite Pluton in Eastern Xinjiang, NW China and its Zoning. *J. Asian Earth Sci.* 42 (5), 885–902. doi:10.1016/j.jseaes.2010.12.010

Han, C., Xiao, W., Su, B., Sakyi, P. A., Ao, S., Zhang, J., et al. (2018). Geology, Re-Os and U-Pb Geochronology and Sulfur Isotope of the the Donggebi Porphyry Mo deposit, Xinjiang, NW China, Central Asian Orogenic Belt. *J. Asian Earth Sci.* 165, 270–284. doi:10.1016/j.jseaes.2018.05.001

Han, C., Xiao, W., Zhao, G., Sun, M., Qu, W., and Du, A. (2014). Re-Os Geochronology on Molybdenites from the Donggebi Mo Deposit in the Eastern Tianshan of the Central Asia Orogenic Belt and its Geological Significance. *Resource Geology.* 64, 136–148. doi:10.1111/rge.12033

Han, J., Chen, H., Hollings, P., Jiang, H., Xu, H., Zhang, L., et al. (2019). The Formation of Modified Zircons in F-Rich Highly-Evolved Granites: An Example from the Shuangji Granites in Eastern Tianshan, China. *Lithos* 324-325, 776–788. doi:10.1016/j.lithos.2018.12.009

Han, J., Chen, H., Hollings, P., Wang, J., Zhang, D., Zhang, L., et al. (2021). Efficient Enrichment of Rb during the Magmatic-Hydrothermal Transition in a Highly Evolved Granitic System: Implications from Mica Chemistry of the Tiantangshan Rb-Sn-W deposit. *Chem. Geology.* 560, 120020. doi:10.1016/j.chemgeo.2020.120020

Hanchar, J. M., and Van Westrenen, W. (2007). Rare Earth Element Behavior in Zircon-Melt Systems. *Elements* 3 (1), 37–42. doi:10.2113/gselements.3.1.37

Harley, S. L., Kelly, N. M., and Moller, A. (2007). Zircon Behaviour and the Thermal Histories of Mountain Chains. *Elements* 3 (1), 25–30. doi:10.2113/gselements.3.1.25

Hildreth, W. (1981). Gradients in Silicic Magma chambers: Implications for Lithospheric Magmatism. *J. Geophys. Res.* 86 (B11), 10153–10192. doi:10.1029/jb086ib11p10153

Hoskin, P. W. O. (2005). Trace-element Composition of Hydrothermal Zircon and the Alteration of Hadean Zircon from the Jack Hills, Australia. *Geochimica et Cosmochimica Acta* 69 (3), 637–648. doi:10.1016/j.gca.2004.07.006

Hou, T., Zhang, Z., Santosh, M., Encarnacion, J., Zhu, J., and Luo, W. (2014). Geochronology and Geochemistry of Submarine Volcanic Rocks in the Yamansu Iron deposit, Eastern Tianshan Mountains, NW China: Constraints on the Metallogenesis. *Ore Geology. Rev.* 56, 487–502. doi:10.1016/j.oregeorev.2013.03.008

Hu, A., Wang, Z., and Tu, G. (1997). *Geological Evolution, Petrogenesis and Metallogeny of North Xinjiang*. Beijing: Science Press. (in Chinese).

Huang, W., Wu, J., Liang, H., Zhang, J., Ren, L., and Chen, X. (2020). Ages and Genesis of W-Sn and Ta-Nb-Sn-W Mineralization Associated with the Limu Granite Complex, Guangxi, China. *Lithos* 352-353, 105321. doi:10.1016/j.lithos.2019.105321

Irber, W. (1999). The Lanthanide Tetrad Effect and its Correlation with K/Rb, Eu/Eu*, Sr/Eu, Y/Ho, and Zr/Hf of Evolving Peraluminous Granite Suites. *Geochimica et Cosmochimica Acta* 63 (3-4), 489–508. doi:10.1016/s0016-7037(99)00027-7

Jackson, S. E., Pearson, N. J., Griffin, W. L., and Belousova, E. A. (2004). The Application of Laser Ablation-Inductively Coupled Plasma-Mass Spectrometry to *In Situ* U-Pb Zircon Geochronology. *Chem. Geology.* 211, 47–69. doi:10.1016/j.chemgeo.2004.06.017

Jahn, B.-M. (2004). The Central Asian Orogenic Belt and Growth of the continental Crust in the Phanerozoic. *Geol. Soc. Lond. Spec. Publications* 226 (1), 73–100. doi:10.1144/gsl.sp.2004.226.01.05

Jia, Z. L. (2016). *Geochemical and Metallogenetical Characteristics of Nb-Ta-Rb Deposits, South Qilian-Beishan Area*. Gansu Province, China: Lanzhou University. (in Chinese).

Jiang, W.-C., Li, H., Turner, S., Zhu, D.-P., and Wang, C. (2020). Timing and Origin of Multi-Stage Magmatism and Related W-Mo-Pb-Zn-Fe-Cu Mineralization in the Huangshaping deposit, South China: An Integrated Zircon Study. *Chem. Geology.* 552, 119782. doi:10.1016/j.chemgeo.2020.119782

Kusiak, M. A., Dunkley, D. J., Slaby, E., Martin, H., and Budzyn, B. (2009). Sensitive High-Resolution Ion Microprobe Analysis of Zircon Reequilibrated by Late Magmatic Fluids in a Hybridized Pluton. *Geology* 37 (12), 1063–1066. doi:10.1130/g30048a.1

Lei, R. X., Wu, C. Z., Zhang, Z. Z., Gu, L. X., Tang, J. H., and Li, G. R. (2013). Geochronology, Geochemistry and Tectonic Significances of the Yamansubei Pluton in Eastern Tianshan, Northwest China. *Acta Petrologica Sinica* 29 (8), 2653–2664. (in Chinese).

Lei, R.-X., Brzozowski, M. J., Feng, Y.-g., Zhang, K., Muhtar, M. N., Luo, X., et al. (2020). Triassic Crust-Mantle Interaction in the Eastern Tianshan, Southern Altaids: Insights from Microgranular Enclaves and Their Host Tianhu Granitoids. *Lithos*, 105879. doi:10.1016/j.lithos.2020.105879

Lei, R.-X., Wu, C.-Z., Gu, L.-X., Zhang, Z.-Z., Chi, G.-X., and Jiang, Y.-H. (2011). Zircon U-Pb Chronology and Hf Isotope of the Xingxingxia Granodiorite from the Central Tianshan Zone (NW China): Implications for the Tectonic Evolution of the Southern Altaids. *Gondwana Res.* 20 (2), 582–593. doi:10.1016/j.gr.2011.02.010

Li, H., Chen, F., Lu, Y., Yang, H., Guo, J., and Mei, Y. (2005). New Chronological Evidence for Indosinian Diagenetic Mineralization in Eastern Xinjiang, NW China. *Acta Geologica Sinica* 79 (2), 264–275.

Li, H., Wu, J.-H., Evans, N. J., Jiang, W.-C., and Zhou, Z.-K. (2018). Zircon Geochronology and Geochemistry of the Xianghualing A-type Granitic Rocks: Insights into Multi-Stage Sn-Polymetallic Mineralization in South China. *Lithos* 312-313, 1–20. doi:10.1016/j.lithos.2018.05.001

Li, T. G., Liang, M. H., Yu, J. P., Huang, Z. B., and Zhang, X. (2018). *Geological Background of Rare (Rare-earth) Matal Mineralization in Gansu Province*. Beijing: Geological Publishing House. (in Chinese).

Li, X.-C., Zhou, M.-F., Chen, W. T., Zhao, X.-F., and Tran, M. (2018). Uranium-lead Dating of Hydrothermal Zircon and Monazite from the Sin Quyen Fe-Cu-REE-Au-(U) deposit, Northwestern Vietnam. *Miner Deposita* 53 (3), 399–416. doi:10.1007/s00126-017-0746-4

Li, N., Yang, F., Zhang, Z., and Yang, C. (2019). Geochemistry and Chronology of the Biotite Granite in the Xiaobaishitou W-(Mo) deposit, Eastern Tianshan, China: Petrogenesis and Tectonic Implications. *Ore Geology. Rev.* 107, 999–1019. doi:10.1016/j.oregeorev.2019.03.027

Li, S., Chung, S. L., Wilde, S. A., Jahn, B. M., Xiao, W. J., Wang, T., et al. (2017). Early-Middle Triassic High Sr/Y Granitoids in the Southern Central Asian Orogenic Belt: Implications for Ocean Closure in Accretionary Orogens. *J. Geophys. Res. Solid Earth* 122 (3), 2291–2309. doi:10.1002/2017jb014006

Li, W. M., Ren, B. C., Yang, X. K., Li, Y. Z., and Chen, Q. (2002). The Intermediate-Acid Intrusive Magmatism and its Geodynamic Significance in Eastern Tianshan Region. *Northwest. Geology.* 35 (4), 41–64. (in Chinese).

Li, X., and Zhou, M.-F. (2015). Multiple Stages of Hydrothermal REE Remobilization Recorded in Fluorapatite in the Paleoproterozoic Yinachang Fe-Cu-(REE) deposit, Southwest China. *Geochimica et Cosmochimica Acta* 166, 53–73. doi:10.1016/j.gca.2015.06.008

Liu, B., and Wang, X. (2016). SIMS U-Pb Dating and Hf Isotope of Zircons from the Deep Granite Porphyry in Baishan Mo deposit, Eastern Tianshan, Northwest China, and Their Geological Significance. *Earth Sci. Front.* 23 (05), 291–300. doi:10.13745/j.esf.2016.05.028

Liu, S. H., Wu, C. Z., Gu, L. X., Zhang, Z. Z., Tang, J. H., Li, G. R., et al. (2008). Geochronology, Petrogenesis and Tectonic Signififfcances of the Baishitouquan Pluton in Middle Tianshan, Northwest China. *Acta Petrologica Sinica* 24, 2720–2730. (in Chinese).

Liu, Y., Hou, Z., Zhang, R., Wang, P., Gao, J., and Raschke, M. B. (2019). Zircon Alteration as a Proxy for Rare Earth Element Mineralization Processes in Carbonatite-Nordmarkite Complexes of the Mianning-Dechang Rare Earth Element Belt, China. *Econ. Geology.* 114 (4), 719–744. doi:10.5382/econgeo.4660

Ludwig, K. W. (2008). *User's Manual for Isoplot 3.70. In A Geochronological Toolkit for Microsoft Excel*. California: Berkeley Geochronology Center Special Publication, 4 76.

Masuda, A., and Ikeuchi, Y. (1979). Lanthanide Tetrad Effect Observed in marine Environment. *Geochem. J.* 13, 19–22. doi:10.2343/geochemj.13.19

Miller, J. S., Matzel, J. E. P., Miller, C. F., Burgess, S. D., and Miller, R. B. (2007). Zircon Growth and Recycling during the Assembly of Large, Composite Arc Plutons. *J. Volcanology Geothermal Res.* 167 (1), 282–299. doi:10.1016/j.jvolgeores.2007.04.019

Monecke, T., Dulski, P., and Kempe, U. (2007). Origin of Convex Tetrads in Rare Earth Element Patterns of Hydrothermally Altered Siliceous Igneous Rocks from the Zinnwald Sn-W deposit, Germany. *Geochimica et Cosmochimica Acta* 71, 335–353. doi:10.1016/j.gca.2006.09.010

Monecke, T., Kempe, U., Monecke, J., Sala, M., and Wolf, D. (2002). Tetrad Effect in Rare Earth Element Distribution Patterns: a Method of Quantification with Application to Rock and mineral Samples from Granite-Related Rare Metal Deposits. *Geochimica et Cosmochimica Acta* 66, 1185–1196. doi:10.1016/s0016-7037(01)00849-3

Muhtar, M. N., Wu, C. Z., Santosh, M., Lei, R. X., Gu, L. X., Wang, S. M., et al. (2020b). Late Paleozoic Tectonic Transition from Subduction to post-collisional Extension in Eastern Tianshan, Central Asian Orogenic Belt. *GSA Bull.* 132 (7-8), 1756–1774. doi:10.1130/b35432.1

Muhtar, M. N., Wu, C. Z., Santosh, M., Lei, R. X., Feng, Y., Yang, T., et al. (2020a). Peraluminous Granitoid Magmatism from Isotopically Depleted Sources: The Case of Jing'erquanbei Pluton in Eastern Tianshan, Northwest China. *Geol. J.* 55 (1), 117–132. doi:10.1002/gj.3392

Nasdala, L., Pidgeon, R. T., and Wolf, D. (1996). Heterogeneous Metamictization of Zircon on a Microscale. *Geochimica et Cosmochimica Acta* 60 (6), 1091–1097. doi:10.1016/0016-7037(95)00454-8

Nasdala, L., Wenzel, M., Vavra, G., Irmer, G., Wenzel, T., and Kober, B. (2001). Metamictisation of Natural Zircon: Accumulation versus thermal Annealing of Radioactivity-Induced Damage. *Contrib. Mineral. Petrol.* 141 (2), 125–144. doi:10.1007/s004100000235

Ostrooumov, M. (2015). *Amazonite: Mineralogy, Crystal Chemistry, and Typomorphism*. Elsevier.

Palenick, C. S., Nasdala, L., and Ewing, R. C. (2003). Radiation Damage in Zircon. *Am. Mineral.* 88 (5-6), 770–781. doi:10.2138/am-2003-5-606

Pupin, J. P. (2000). Granite Genesis Related to Geodynamics from Hf-Y in Zircon. *Earth Environ. Sci. Trans. R. Soc. Edinb.* 91 (1-2), 245–256. doi:10.1017/s0263593300007410

Rubin, J. N., Henry, C. D., and Price, J. G. (1993). The Mobility of Zirconium and Other "immobile" Elements during Hydrothermal Alteration. *Chem. Geology.* 110 (1-3), 29–47. doi:10.1016/0009-2541(93)90246-f

Seltmann, R., Soloviev, S., Shatov, V., Pirajno, F., Naumov, E., and Cherkasov, S. (2010). Metallogeny of Siberia: Tectonic, Geologic and Metallogenic Settings of Selected Significant Deposits*. *Aust. J. Earth Sci.* 57 (6), 655–706. doi:10.1080/08120099.2010.505277

Sengor, A. M. C., and Natal'in, B. A. (1996). "Paleotectonics of Asia: Frangments of Synthesis," in *The Tectonic Evolution of Asia*. Editors A. Yin and T. M. Harrison (Cambridge: Cambridge University Press), 480–640.

Sengor, A., Natal'in, B., and Burtman, V. (1993). Evolution of the Altaid Tectonic Collage and Palaeozoic Crustal Growth in Eurasia. *Nature* 364 (6435), 299–307. doi:10.1038/364299a0

Shu, L., Wang, B., Zhu, W., Guo, Z., Charvet, J., and Zhang, Y. (2011). Timing of Initiation of Extension in the Tianshan, Based on Structural, Geochemical and Geochronological Analyses of Bimodal Volcanism and Olistostrome in the Bogda Shan (NW China). *Int. J. Earth Sci. (Geol Rundsch)* 100 (7), 1647–1663. doi:10.1007/s00531-010-0575-5

Shu, L., Yu, J., Charvet, J., Laurent-Charvet, S., Sang, H., and Zhang, R. (2004). Geological, Geochronological and Geochemical Features of Granulites in the Eastern Tianshan, NW China. *J. Asian Earth Sci.* 24 (1), 25–41. doi:10.1016/j.jseaes.2003.07.002

Smith, D., Jorre, L., Reed, S., and Long, J. (1991). Zonally Metamictized and Other Zircons from Thor Lae, Northwest Territories. *Can. mineral* 29, 301–309.

Sun, H., Li, H., Danišík, M., Xia, Q., Jiang, C., Wu, P., et al. (2017). U-pb and Re-os Geochronology and Geochemistry of the Donggebi Mo deposit, Eastern Tianshan, NW China: Insights into Mineralization and Tectonic Setting. *Ore Geology. Rev.* 86, 584–599. doi:10.1016/j.oregeorev.2017.03.020

Sun, Y. (2013). *Research on of Typical Rubidium Deposits and Tectonic Background in China*. Beijing, China: China University of Geosciences. (in Chinese). doi:10.4324/9781315878560

Takahashi, Y., Yoshida, H., Sato, N., Hama, K., Yusa, Y., and Shimizu, H. (2002). W- and M-type Tetrad Effects in REE Patterns for Water-Rock Systems in the Tono Uranium deposit, central Japan. *Chem. Geology.* 184 (3-4), 311–335. doi:10.1016/s0009-2541(01)00388-6

Takehara, M., Horie, K., Hokada, T., and Kiyokawa, S. (2018). New Insight into Disturbance of U-Pb and Trace-Element Systems in Hydrothermally Altered Zircon via SHRIMP Analyses of Zircon from the Duluth Gabbro. *Chem. Geology.* 484, 168–178. doi:10.1016/j.chemgeo.2018.01.028

Tang, Y., and Zhang, H. (2015). Lanthanide Tetrads in Normalized Rare Element Patterns of Zircon from the Koktokay No. 3 Granitic Pegmatite, Altay, NW China. *Am. Mineral.* 100 (11-12), 2630–2636. doi:10.2138/am-2015-5270

Van Achterbergh, E., Ryan, C. G., Jackson, S. E., and Griffin, W. L. (2001). "Data Reduction Software for LA–ICP–MS: Appendix," in *Laser Ablation–ICP–Mass Spectrometry in the Earth Sciences. Principles and Applications, Mineralogical Association of Canada (MAC) Short Course Series*. Editor P. J. Sylvester (Ottawa, Ontario: Canada), 239–243.

Van Lichtervelde, M., Melcher, F., and Wirth, R. (2009). Magmatic vs. Hydrothermal Origins for Zircon Associated with Tantalum Mineralization in the Tanco Pegmatite, Manitoba, Canada. *Am. Mineral.* 94 (4), 439–450. doi:10.2138/am.2009.2952

Veksler, I. V., Dorfman, A. M., Kamenetsky, M., Dulski, P., and Dingwell, D. B. (2005). Partitioning of Lanthanides and Y between Immiscible Silicate and Fluoride Melts, Fluorite and Cryolite and the Origin of the Lanthanide Tetrad Effect in Igneous Rocks. *Geochimica et Cosmochimica Acta* 69 (11), 2847–2860. doi:10.1016/j.gca.2004.08.007

Veksler, I. V. (2004). Liquid Immiscibility and its Role at the Magmatic-Hydrothermal Transition: a Summary of Experimental Studies. *Chem. Geology.* 210 (1-4), 7–31. doi:10.1016/j.chemgeo.2004.06.002

Wang, B., Cluzel, D., Jahn, B.-m., Shu, L., Chen, Y., Zhai, Y., et al. (2014). Late Paleozoic Pre- and Syn-Kinematic Plutons of the Kangguer-Huangshan Shear Zone: Inference on the Tectonic Evolution of the Eastern Chinese north Tianshan. *Am. J. Sci.* 314 (1), 43–79. doi:10.2475/01.2014.02

Wang, J. B., Wang, Y. W., and He, Z. H. (2006). Ore Deposits as a Guide to the Tectonic Evolution in the East Tianshan Mountains, NW China. *Geology. China* 33, 461–469. (in Chinese).

Wang, R., Cheng Che, X., Dong Zhang, W., Lan Zhang, A., and Cheng Zhang, H. (2009). Geochemical Evolution and Late Re-equilibration of NaCs-Rich Beryl from the Koktokay #3 Pegmatite (Altai, NW China). *ejm* 21 (4), 795–809. doi:10.1127/0935-1221/2009/0021-1936

Wang, X., Griffin, W. L., Chen, J., Huang, P. Y., and Li, X. (2011). U and Th Contents and Th/U Ratios of Zircon in Felsic and Mafic Magmatic Rocks: Improved Zircon–Melt Distribution Coefficients. *Acta Geol. Sinica (English Edition)* 85 (1), 164–174.

Wang, X., Chen, J., and Ren, M. (2016). Hydrothermal Zircon Geochronology: Age Constraint on Nanling Range Tungsten Mineralization (Southeast China). *Ore Geology. Rev.* 74, 63–75. doi:10.1016/j.oregeorev.2015.10.034

Wang, X., Griffin, W. L., and Chen, J. (2010). Hf Contents and Zr/Hf Ratios in Granitic Zircons. *Geochem. J.* 44 (1), 65–72. doi:10.2343/geochemj.1.0043

Wang, X., and Ren, M. (2018). Constraints of Hydrothermal and Magmatic Zircon on the Origin of the Yaogangxian Tungsten deposit, Southern China. *Ore Geology. Rev.* 101, 453–467. doi:10.1016/j.oregeorev.2018.07.011

Wang, Y. H., Zhang, F. F., Liu, J. J., Xue, C. J., Wang, J. P., Liu, B., et al. (2015). Petrogenesis of Granites in Baishan Molybdenum deposit, Eastern Tianshan, Xinjiang: Zircon U-Pb Geochronology, Geochemistry, and Hf Isotope Constraints. *Acta Petrologica Sinica* 31 (7), 1962–1976. (in Chinese).

Wang, Y. S., Zou, H., Tu, Q. J., Xu, M., Yang, C., and Fu, Y. Z. (2019). Zircon U-Pb and Molybdenite Re-os Geochronology and Whole-rock Geochemistry of the Baishan Porphyry Mo deposit: Insights into Triassic Mineralisation and Tectonic Setting in the Eastern Tianshan, NW China. *Geol. J.* 55 (6), 4057–4078. doi:10.1002/gj.3654

Wang, Y. W., Wang, J. B., Wang, L. J., and Long, L. L. (2008). Zircon U-Pb Age, Sr-Nd Isotope Geochemistry and Geological Significances of the Weiya Mafic-Ultramafic Complex, Xinjiang. *Acta Petrologica Sinica* 24 (4), 781–792. (in Chinese).

Wang, Y.-h., Zhang, F.-f., Liu, J.-j., Xue, C.-j., Li, B.-c., and Xian, X.-c. (2018). Ore Genesis and Hydrothermal Evolution of the Donggebi Porphyry Mo Deposit, Xinjiang, Northwest China: Evidence from Isotopes (C, H, O, S, Pb), Fluid Inclusions, and Molybdenite Re-os Dating. *Econ. Geology.* 113 (2), 463–488. doi:10.5382/econgeo.2018.4558

Wang, Y., Chen, H., Han, J., Chen, S., Huang, B., Li, C., et al. (2018). Paleozoic Tectonic Evolution of the Dananhu-Tousuquan Island Arc belt, Eastern Tianshan: Constraints from the Magmatism of the Yuhai Porphyry Cu deposit, Xinjiang, NW China. *J. Asian Earth Sci.* 153, 282–306. doi:10.1016/j.jseaes.2017.05.022

Wang, Y., Xue, C., Liu, J., and Zhang, F. (2016). Geological, Geochronological, Geochemical, and Sr-Nd-O-Hf Isotopic Constraints on Origins of Intrusions Associated with the Baishan Porphyry Mo deposit in Eastern Tianshan, NW China. *Miner Deposita* 51 (7), 953–969. doi:10.1007/s00126-016-0646-z

Wasilewski, P. J., Senftle, F. E., Vaz, J. E., Thorpe, A. N., and Alexander, C. C. (1973). A Study of the Natural α-recoil Damage in Zircon by Infrared Spectra. *Radiat. Effects* 17 (3-4), 191–199. doi:10.1080/00337577308232615

Weber, W. J., Ewing, R. C., and Wang, L.-M. (1994). The Radiation-Induced Crystalline-To-Amorphous Transition in Zircon. *J. Mater. Res.* 9 (3), 688–698. doi:10.1557/jmr.1994.0688

Webster, J. D., and Holloway, J. R. (1990). Partitioning of F and Cl between Magmatic Hydrothermal Fluids and Highly Evolved Granitic Magmasfluids and Highly Evolved Granitic Magmas. *Geol. Soc. America Spec. Paper* 246, 21–34. doi:10.1130/spe246-p21

Wilkinson, J. J. (2001). Fluid Inclusions in Hydrothermal Ore Deposits. *Lithos* 55 (1-4), 229–272. doi:10.1016/s0024-4937(00)00047-5

Windley, B. F., Alexeiev, D., Xiao, W., Kröner, A., and Badarch, G. (2007). Tectonic Models for Accretion of the Central Asian Orogenic Belt. *J. Geol. Soc.* 164 (1), 31–47. doi:10.1144/0016-76492006-022

Wu, C.-z., Liu, S.-h., Gu, L.-x., Zhang, Z.-z., and Lei, R.-x. (2011). Formation Mechanism of the Lanthanide Tetrad Effect for a Topaz- and Amazonite-Bearing Leucogranite Pluton in Eastern Xinjiang, NW China. *J. Asian Earth Sci.* 42 (5), 903–916. doi:10.1016/j.jseaes.2010.09.011

Wu, C.-Z., Xie, S.-W., Gu, L.-X., Samson, I. M., Yang, T., Lei, R.-X., et al. (2018). Shear Zone-Controlled post-magmatic Ore Formation in the Huangshandong Ni-Cu Sulfide deposit, NW China. *Ore Geology. Rev.* 100, 545–560. doi:10.1016/j.oregeorev.2017.02.015

Wu, C.-Z., Zhang, Z.-Z., Gu, L.-X., Tang, J.-H., and Lei, R.-X. (2010). Sr, Nd and O Isotopic Characters of Quartz Syenite in the Weiya Magmatic Complex from Eastern Tianshan in NW China: Melting of the Thickened Juvenile Lower Crust. *Geochem. J.* 44 (4), 285–298. doi:10.2343/geochemj.1.0072

Wu, Y. S., Xiang, N., Tang, H. S., Zhou, K. F., and Yang, Y. F. (2013). Molybdenite Re-os Isotope Age of the Donggebi Mo deposit and the Indosinian Metallogenic Event in Eastern Tianshan. *Acta Petrologica Sinica* 29 (1), 121–130. (in Chinese).

Wu, Y.-S., Zhou, K.-F., Li, N., and Chen, Y.-J. (2017). Zircon U-Pb Dating and Sr-Nd-Pb-Hf Isotopes of the Ore-Associated Porphyry at the Giant Donggebi Mo deposit, Eastern Tianshan, NW China. *Ore Geology. Rev.* 81, 794–807. doi:10.1016/j.oregeorev.2016.02.007

Xiao, W.-J., Zhang, L. C., Qin, K. Z., Sun, S. H. U., and Li, J. L. (2004). Paleozoic Accretionary and Collisional Tectonics of the Eastern Tianshan (China): Implications for the continental Growth of central Asia. *Am. J. Sci.* 304 (4), 370–395. doi:10.2475/ajs.304.4.370

Xiao, W., Windley, B. F., Sun, S., Li, J., Huang, B., Han, C., et al. (2015). A Tale of Amalgamation of Three Permo-Triassic Collage Systems in Central Asia: Oroclines, Sutures, and Terminal Accretion. *Annu. Rev. Earth Planet. Sci.* 43 (1), 477–507. doi:10.1146/annurev-earth-060614-105254

Xu, X.-W., Ma, T.-L., Sun, L.-Q., and Cai, X.-P. (2003). Characteristics and Dynamic Origin of the Large-Scale Jiaoluotage Ductile Compressional Zone in the Eastern Tianshan Mountains, China. *J. Struct. Geology.* 25 (11), 1901–1915. doi:10.1016/s0191-8141(03)00017-8

Xu, Y. X., Qin, K. Z., Ding, K. S., Li, J. X., Miao, Y., Fang, T. H., et al. (2008). Geochronology Evidence of Mesozoic Metallogenesis and Cenozoic Oxidation at Hongshan HS-Epithermal Cu-Au deposit, Kalatage Region, Eastern Tianshan, and its Tectonic and Paleoclimatic Significances. *Acta Petrologica Sinica* 24 (10), 2371–2383. (in Chinese).

Yang, W.-B., Niu, H.-C., Shan, Q., Sun, W.-D., Zhang, H., Li, N.-B., et al. (2014). Geochemistry of Magmatic and Hydrothermal Zircon from the Highly Evolved Baerzhe Alkaline Granite: Implications for Zr-REE-Nb Mineralization. *Miner Deposita* 49, 451–470. doi:10.1007/s00126-013-0504-1

Zhang, D. Y., Zhou, T. F., Yuan, F., Fan, Y., Liu, S., and Qu, W. J. (2009). A Genetic Analysis of Baishan Molybdenum deposit in East Tianshan Area , Xinjiang. *Mineral. Deposits* 5, 152–161. (in Chinese). doi:10.3969/j.issn.0258-7106.2009.05.012

Zhang, D., Zhou, T., Yuan, F., Fan, Y., Deng, Y., Xu, C., et al. (2014). Genesis of Permian Granites along the Kangguer Shear Zone, Jueluotage Area, Northwest China: Geological and Geochemical Evidence. *Lithos* 198-199, 141–152. doi:10.1016/j.lithos.2014.03.023

Zhang, D., Zhou, T., Yuan, F., Xiao, W., White, N. C., Deng, Y., et al. (2015). Petrogenesis and Mineralization Potential of a Granite Porphyry Intrusion beneath the Baishan Mo deposit, Eastern Tianshan, NW China. *J. Asian Earth Sci.* 113, 254–265. doi:10.1016/j.jseaes.2015.05.002

Zhang, F., Wang, Y., Liu, J., and Wang, J. (2015). Zircon U-Pb and Molybdenite Re-Os Geochronology, Hf Isotope Analyses, and Whole-Rock Geochemistry of the Donggebi Mo deposit, Eastern Tianshan, Northwest China, and Their Geological Significance. *Int. Geology. Rev.* 57 (4), 446–462. doi:10.1080/00206814.2015.1013067

Zhang, L., Xiao, W., Qin, K., Qu, W., and Du, A. (2005). Re-Os Isotopic Dating of Molybdenite and Pyrite in the Baishan Mo?Re deposit, Eastern Tianshan, NW China, and its Geological Significance. *Miner Deposita* 39 (8), 960–969. doi:10.1007/s00126-004-0451-y

Zhang, W., Chen, H., Han, J., Zhao, L., Huang, J., Yang, J., et al. (2016). Geochronology and Geochemistry of Igneous Rocks in the Bailingshan Area: Implications for the Tectonic Setting of Late Paleozoic Magmatism and Iron Skarn Mineralization in the Eastern Tianshan, NW China. *Gondwana Res.* 38, 40–59. doi:10.1016/j.gr.2015.10.011

Zhang, X., Zhao, G., Sun, M., Han, Y., and Liu, Q. (2017). Triassic Magmatic Reactivation in Eastern Tianshan, NW China: Evidence from Geochemistry and Zircon U-Pb-Hf Isotopes of Granites. *J. Asian Earth Sci.* 145, 446–459. doi:10.1016/j.jseaes.2017.06.022

Zhang, Z. Z., Gu, L. X., Wu, C. Z., Li, W. Q., Xi, A. H., and Wang, S. (2005). Zircon SHRIMP Dating for the Weiya Pluton, Eastern Tianshan: Its Geological Implications. *Acta Geologica Sinica* 79 (4), 481–490. doi:10.1111/j.1755-6724.2005.tb00914.x

Zhao, H. G., Su, R., Liang, J. W., Wang, J., Jin, Y. X., Ou, G. X., et al. (2017). Petrology, Geochemical Characteristics and Genesis of the Tianhu Pluton in the East Section of the Middle Tianshan Moutains. *Acta Geologica Sinica* 91 (06), 1208–1226. (in Chinese). doi:10.1111/1755-6724.13405

Zhao, L., Chen, H., Hollings, P., and Han, J. (2019). Tectonic Transition in the Aqishan-Yamansu belt, Eastern Tianshan: Constraints from the Geochronology and Geochemistry of Carboniferous and Triassic Igneous Rocks. *Lithos* 344-345, 247–264. doi:10.1016/j.lithos.2019.06.023

Zhao, Z. H., Xiong, X. L., Wang, Q., and Qiao, Y. L. (2008). Some Aspects on Geochemistry of Nb and Ta. *Geochimica* 37 (4), 304–320. (in Chinese).

Zhou, T. F., Yuan, F., Zhang, D. Y., Fan, Y., Liu, S., Peng, M. X., et al. (2010). Geochronology, Tectonic Setting and Mineralization of Granitoids in Jueluotage Area, Eastern Tianshan, Xinjiang. *Acta Petrologica Sinica* 26 (2), 478–502. (in Chinese).

Conflict of Interest: The authors declare that the research was conducted in the absence of any commercial or financial relationships that could be construed as a potential conflict of interest.